J. Fluid Mech. (1996), *vol.* 307, *pp.* 297–331

Convection in ^{3}He–superfluid-^{4}He mixtures. Part 2. A survey of instabilities

By GUY METCALFE[1] AND R. P. BEHRINGER[2]

[1]Division of Building, Construction and Engineering, CSIRO, Highett 3190, Australia

[2]Duke University Department of Physics and Center for Nonlinear and Complex Systems, Durham, NC 27708, USA

(Received 13 October 1994 and in revised form 20 September 1995)

Dilute mixtures of ^{3}He in superfluid ^{4}He have Prandtl numbers easily tunable between those of liquid metals and water: $0.04 < Pr < 2$. Moreover, superfluid mixture convection is closely analogous to classical Rayleigh–Bénard convection, i.e. superfluid mixtures convect as if they were classical, single-component fluids. This work has two goals. The first, accomplished in Part 1, is to experimentally validate the superfluid mixture convection analogue to Rayleigh–Bénard convection.

With superfluid effects understood and under control, the second goal is to identify and characterize time-dependence and chaos and to discover new dynamical behaviour in strongly nonlinear convective flows. In this paper, Part 2, we exploit the unique Pr range of superfluid mixtures and the variable aspect ratio (Γ) capabilities of our experiment to survey convective instabilities in the broad, and heretofore largely unexplored, parameter space $0.12 < Pr < 1.4$ and $2 < \Gamma < 95$. Within this large parameter space, we have focused on small to moderate Γ and Pr and on large Γ with $Pr \approx 1$. The novel behaviour uncovered in the survey includes the following. *Changing attractors*: at $\Gamma = 6.0$ and $Pr = 0.3$, we observe intermittent bursting destabilizing a fully developed chaotic state. Above the onset of bursting the average length of a burst-free interval and the average length of a burst vary as power laws. At $\Gamma = 4.25$ and $Pr = 0.12$ we observe a particularly novel reversible switching transition involving two chaotic attractors. *Instability competition*: near the codimension-2 point at the crossing of the skewed-varicose and oscillatory instabilities we find that the effects of instability competition greatly increase the complexity and multiplicity of states. A heat-pulse method allows selection of the active state. Decreasing Γ suppresses the available complexity. *Superfluid turbulence*: we find that the large-amplitude noisy states, previously believed due to superfluid turbulence, are confined to small values of Γ and Pr and are not consistent with superfluid turbulence. *Changing instabilities*: at $Pr = 0.19$ a wavevector detuning changes the type of secondary instability from oscillatory to saddle-node, with an unusual 3/4 exponent time scaling. *Very large* Γ: at $Pr = 1.3$ for Γ increasing from 44 to 90, we observe the onset of convection changing from ordered and stationary to disordered and time-dependent. At the beginning of the crossover there are hysteretic transitions to coherent oscillations close to the onset of convection. By the end of the crossover convection is time-dependent and irregular at onset with the fluctuation amplitude correlated with the mean Nusselt number.

1. Introduction

The dynamics of Rayleigh–Bénard convection (RBC) rolls has been one of the most valuable experimental arenas for generating and testing ideas on linear and nonlinear stability, dynamical systems, chaos, and the transition to turbulence. As such, the instabilities of RBC rolls have been the subject of intense investigation for nearly 20 years. Two of the important parameters governing the character of these instabilities are the Prandtl number Pr, which is a ratio of thermal to vortical relaxation times, and the aspect ratio Γ, which governs the geometric arrangement and number of rolls. Other relevant parameters are the Rayleigh number Ra, the driving force of the flow, and the roll wavevector q. The Nusselt number N describes the thermal responses of the fluid layer. Variables, parameters, and non-dimensional groups are precisely defined in Part 1 of this work (Metcalfe & Behringer 1996).

No conventional fluid allows continuous experimental exploration of RBC instabilities at low to moderate Pr ($Pr \lesssim 1$). Yet, the instabilities and dynamics of convection rolls are expected to change dramatically over this range (Busse 1981). Conventional fluids, such as water, liquid metals, pure liquid ^{3}He or ^{4}He, and all gases, fall in or near this range of Pr but do not cover it well enough to allow a continuous change of the instabilities which occur after the onset of convection. However, convecting dilute solutions of ^{3}He in superfluid ^{4}He have Prandtl numbers tunable between those of water and liquid metals: $0.04 < Pr < 2$. This makes superfluid mixtures useful for the study of instability and dynamics in highly nonlinear flows. Superfluid mixture convection (SMC) is closely analogous to RBC, and in Part 1 we explored this analogy. Using a combination of theory and experiment, we showed that SMC and RBC differ little as long as the superfluid dissipation length scale $\lambda_\circ \ll d$, where d is the fluid layer height.

Using the apparatus and superfluid mixture described in Part 1, this paper describes experiments to probe and survey convective dynamics over unexplored regions of Γ–Pr space. Figure 1 summarizes the range and variety of phenomena studed in these experiments. The first region we consider is that having low to moderate values of both Pr and Γ. Within this regime, we explore the destabilization of chaotic attractors (§2), the dynamics around the codimension-2 point that occurs where the oscillatory and skew-varicose instabilities intersect (§3), the large-amplitude noisy states seen only at small Γ and Pr (§4), and the effect of wavevector detuning on the oscillatory instability (§5). In the second region (§6) we fix $Pr \approx 1$ and observe the transition with increasing Γ of the onset of convection from stationary to chaotic flow at very large Γ.

2. Chaotic attractor destabilization

The transition to chaos in low-dimensional systems has been extensively documented. As a control parameter is raised, the flow may follow any of several routes to chaos, such as period doubling, quasi-periodicity, intermittency, and boundary crises (Manneville 1990). But, after a chaotic attractor has been established, what is the evolution of the dynamics as the control parameter is further changed? This is an important issue in the study of the transition to turbulence and to date has not been as intensively investigated as the onset of chaos.

In this section we report observations on two ways chaotic attractors destabilize as the control parameter is raised. The first is found at $Pr = 0.30$ and $\Gamma = 6.0$ where a deterministic fully developed chaotic state destabilizes via intermittent bursts.

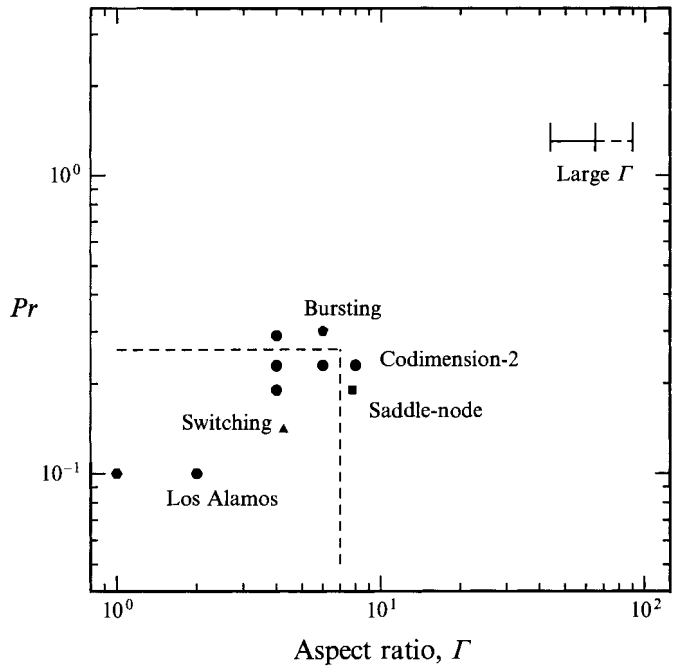

FIGURE 1. Map of aspect ratio–Prandtl number space schematically locating the different phenomena described in the text. The map space delimits the range of Pr and Γ available to our present fluid and apparatus. Of particular note is the large fraction of blank, unexplored space. The dashed line at low aspect ratio is the region in which noisy states are observed; the solid (dashed) line at large aspect ratios indicates steady (noisy) flow near onset. Hexagons indicate representative aspect ratios and Prandtl numbers studied by the Los Alamos group (Haucke *et al.* 1984; Ecke *et al.* 1987).

The system twice postpones fully developed chaos by reregularizing nearly chaotic time series through the elimination of incommensurate frequencies, most probably accompanied by a pattern change. Above the onset of bursting, the average length of a burst-free region and the average length of a burst vary as power laws. The second is found at $Pr = 0.14$ and $\Gamma = 4.25$ where we see a novel reversible switching transition involving two chaotic attractors with different mean Nusselt numbers.

2.1. *Bursting*

The bursting described below should not be confused with the well-known intermittency route to chaos (Pomeau & Manneville 1980). Intermittency, which is well-documented (Bergé *et al.* 1980; Dubois, Rubio & Bergé 1983; Haucke *et al.* 1984) in this and other fluids, is one way a laminar flow can lose stability and *become* chaotic. The bursting described here on the other hand is a way an *already established* chaotic attractor loses stability. Both may occur: intermittency leading to a chaotic attractor followed, upon further increase in the forcing, by the destruction of the attractor via bursting.

2.1.1. *Bifurcations and postponement of chaos*

We consider first how the flow postpones and finally achieves a chaotic state. Figure 2 shows experimental Nusselt data for $\Gamma = 6.0$, $Pr = 0.30$ ($T = 1.302$ K). The downward pointing arrow at $r \equiv Ra/Ra_c = 3.959$ indicates that steady convection terminates in a discontinuous transition to oscillatory convection with a nearly sinusoidal signal. Reduction of r after the transition shrinks the amplitude of oscillations,

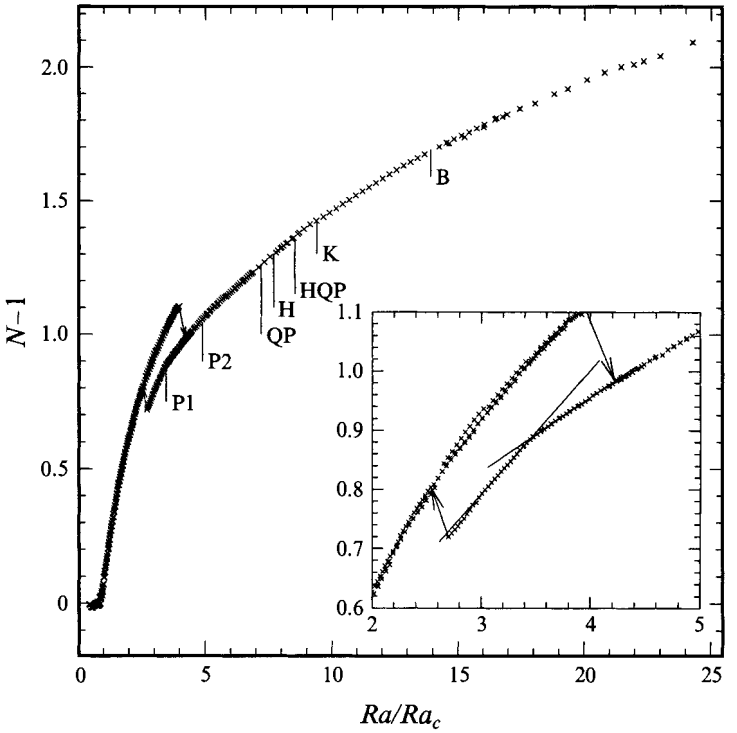

FIGURE 2. Nusselt curve for $Pr = 0.3$, $\Gamma = 6.0$. On the lower-N branch and above $r = 3.456$, convection is time-dependent; all other points show steady convection. Kinks in N at $r = 3.456$ and 9.379 accompany the transitions to respectively period-1 (P1) and knot (K) oscillations. The inset shows on expanded scale the oscillatory instability at $r = 3.456$. The intersection of the straight lines fit to the points above and below the kink in N pinpoint the transition. The labels denote different kinds of time-dependence as discussed in the text: period-2, P2; quasi-periodic, QP; harmonic, H; harmonic quasi-periodic, HQP; and bursting, B.

until at $r = 3.456$ time-dependence stops at the kink in the Nusselt curve, shown enlarged in the inset to figure 2, and steady convection on the lower-N branch begins. With further decrease of r to 2.701, the low-N steady branch jumps back onto the the high-N steady convection branch. The frequency at the onset of oscillations (non-dimentionalized by the vertical thermal diffusion time $\tau_v = 31.4$ s) at $r = 3.456$ is 6.2. At this Prandtl number, the infinite aspect ratio prediction (Clever & Busse 1974) for the oscillatory instability is a frequency of $f\tau_v = 20$ for q at critical $q_c = 3.14$ and 9 for $q = 2.0$.

Although the flow is not visualized, the following scenario accounts for the data. At $r = 3.959$ the skew-varicose instability initiates a wavevector decrease. With only six rolls, losing two of them would change the wavevector to nearly 2. At this Pr the system is close enough to the skew-varicose/oscillatory codimension-2 point (see §3 or Part 1) that a wavevector change to $q \approx 2$ is large enough to push the system completely through the stable region and into the oscillatory region. The jump back onto the initial branch with decreasing r is caused by the system encountering the Eckhaus or zig-zag instability that restores the original wavevector to complete the hysteresis loop. Based on the instability sequence and the frequency, the transition at $r = 3.456$ corresponds to the oscillatory instability of Clever & Busse (Clever & Busse 1974).

The spectral peak at the onset of oscillations remains a prominent feature of the time-dependence for all $r > 3.456$. In order to track and distinguish this peak from other spectral peaks, we will tag it the Busse oscillation peak.

The Nusselt curve in figure 2 and the amplitude and frequency of the Busse oscillation peak in figure 7 show six distinct stages in the evolution of this system before the onset of bursting. Figures 3 and 4 show representative behaviour from each region. Figure 3 shows a time series and the corresponding power spectrum from each region; δT is the deviation from the time-averaged temperature difference across the layer scaled by the temperature difference across the layer at the onset of convection $\Delta T_c = 0.969$ mK. Figure 4 shows a perspective rendering of the time series embedded in 3-space with a delay of $0.051\tau_v$ (4 points); different delays produced no substantive changes. The time series were collected automatically as described in Part 1. Following each change in heat current Q, the experimental control system waited $20\tau_v$–$25\tau_v$ before collecting points; the data rate was 2.5 Hz with a frequency resolution of 1.2 mHz or about $0.04\tau_v$.

At $r = 4.88$ the system period doubles (P2), and at $r = 7.20$ adds a lower incommensurate frequency to become quasi-periodic (QP). At $r = 7.684$ (H) the incommensurate frequency is eliminated and the amplitude of the Busse oscillation peak shrinks while that of the period-doubled peak grows. The frequency ratio between the two peaks is 2/1, but the spectrum appears more like a fundamental with one harmonic than P2. The difference is most evident from the phase portraits. A lower incommensurate frequency reappears at $r = 8.52$ (HQP) and again is eliminated at $r = 9.379$ (K). The new phase portrait makes a trefoil knot: the trajectories departing from one loop pass through the loop on its left and then form the loop on its right. If we label the lowest frequency in the knot spectrum f_1, the rest of the knot spectrum consists of integer multiples if_1, $i = 1,\ldots,10$, with f_1 and f_4, which is the Busse oscillation peak, having the largest amplitudes.

There are two features of this set of transitions to which we would like to draw particular attention. The first is that the system twice postpones the onset of chaos. The following sequence is repeated with increasing Ra as the system goes through the regions QP→H and HQP→K. A sharp commensurate spectrum gains an incommensurate component at lower frequency as r is raised. With further increase in r, a transition to chaos begins, signalled by a broadening of spectral lines and an increase in low-frequency broad-band noise, shown in figure 5. As the level of disorder rises, the original incommensurate frequency is eliminated and the time-dependence reregularizes. The spectral peaks immediately after are again sharp and commensurate, although not the same set of lines as the previous sharp set. The reregularization presumably signals a pattern change. Regularization is apparently not possible a third time and the formation of a strange attractor of high dimension occurs.

The reregularization occurs spontaneously some time after an increase in the heat flux Q and the transitions take place with Q fixed. Figure 6 shows two time records at $r = 7.740$ and 9.379, values at the transitions QP→H and HQP→K respectively. The arrows in the figure suggest the time interval over which the signal changes from one form to another. The transition HQP→K is accompanied by a noticeable kink in the Nusselt curve. No changes in N are discernible for QP→H. There are no indications of hysteresis in the transitions. In figure 6(*a*), about $35\tau_v$ after changing Q, the pattern shifts. (There is about a $20\tau_v$ delay between raising Q and the start of the time record.) In figure 6(*b*) the shift occurs after about $96\tau_v$. That is, the transitions occur about 1 and 3 *horizontal* thermal diffusion times respectively after raising Q. In both cases the change is quick, taking only $4\tau_v$–$5\tau_v$.

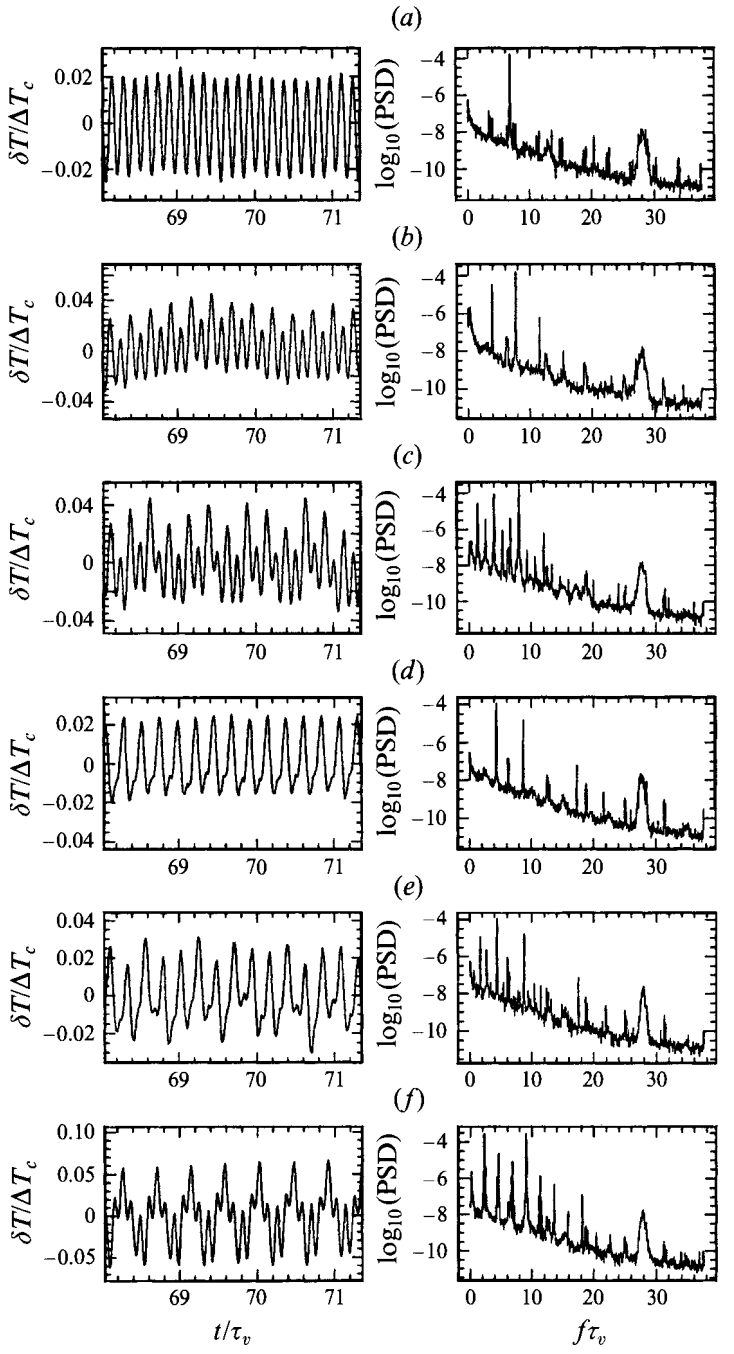

FIGURE 3. Time-dependence at $(Pr, \Gamma) = (0.3, 6.0)$. (*a*) Period-1 $Ra/Ra_c = 4.879$. (*b*) Period-2 $Ra/Ra_c = 7.095$. (*c*) Quasi-periodic $Ra/Ra_c = 7.628$. (*d*) Harmonic oscillation $Ra/Ra_c = 8.406$. (*e*) Quasi-periodic harmonic $Ra/Ra_c = 8.641$. (*f*) Knot oscillation $Ra/Ra_c = 9.653$.

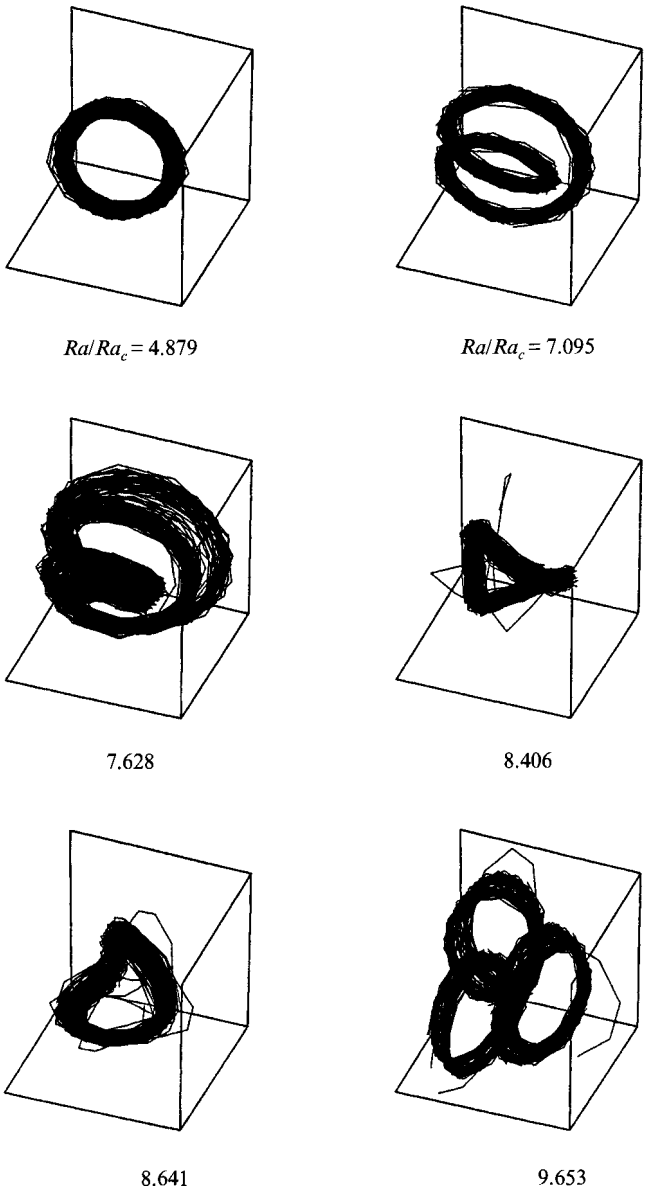

FIGURE 4. Phase portraits from the data of figure 3. Perspective and extent are the same for each portrait, except the last where the length of one side of the box is about $6^{1/3}$ times that of the others.

The second feature of particular interest is that while the Busse oscillation peak remains prominent even into the bursting region, the frequency increases with Ra and the amplitude grows and shrinks. Figure 7 plots the frequency and amplitude of the Busse oscillation peak as a function of $r_O = Ra/Ra_O - 1$, where $Ra_O = 3.959Ra_c$ is the onset of the oscillatory instability. This suggests that rolls oscillating transverse to the local wavevector remain an important Part of the system dynamics, even though the pattern at larger Ra assuredly does not consist of straight rolls.

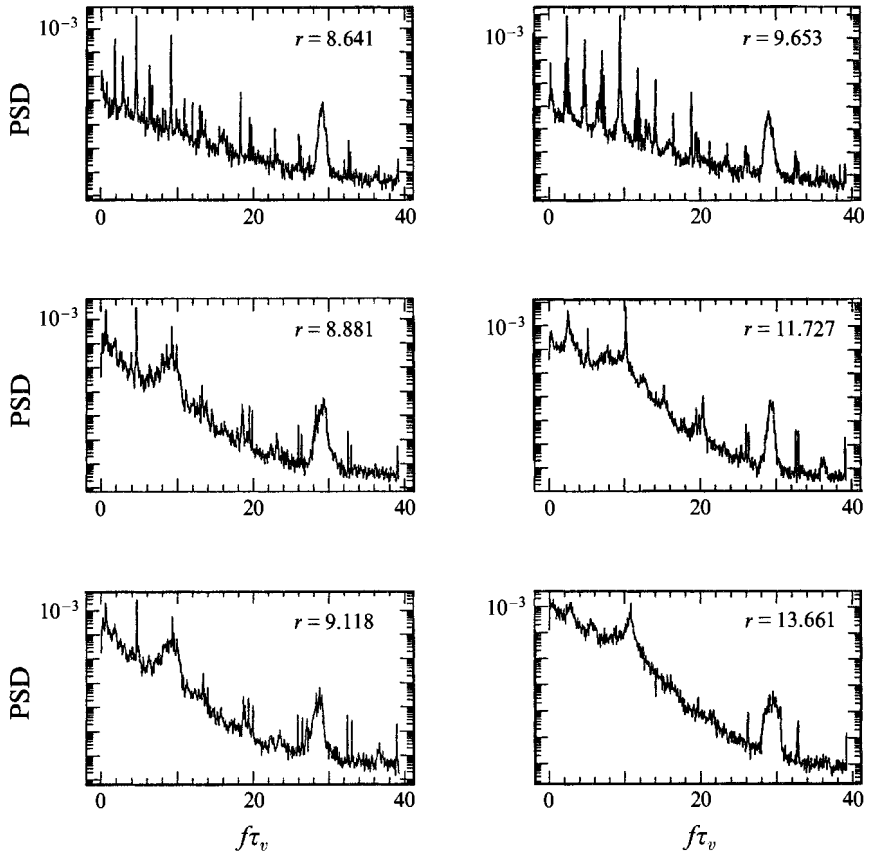

FIGURE 5. Spectra on semi-log scale for the indicated values of r showing how an initially sharp spectrum broadens and the low-frequency broad-band noise rises with increasing r. With further increase in r, though, the fluid returns to a sharp spectrum, having postponed the onset of chaos. The left-hand column shows the region QP→H; the right-hand one shows HQP→K. The broad feature at $f\tau_v = 29$ is an artifact of the temperature control.

The rise in low-frequency broad-band noise occurs simultaneously with an unlocking of frequencies. For example, in the knot region (K) f_1 and f_4 are locked at $r = 9.653$. As r increases these frequencies increase but not at the same rate, so that by $r = 11.727$ $f_4/f_1 = 4.19$. As this unlocking progresses, the low-frequency noise rises.

The final chaotic state before the onset of bursting has an irregular time series with a broad-band spectrum, which is shown on log–log scale in figure 8. This spectral shape – nearly flat for several decades followed by a sharp power-law fall-off – has been seen in several convection experiments (Ahlers & Behringer 1978; Gollub & Benson 1980), although, the fall-off is significantly steeper here than in many experiments. We have also tried to calculate the box dimension d_b of the attractor using the Grassberger–Proccacia algorithm as modified by Theiler (1987) to be more efficient for high-dimensions. The value of d_b obtained by this analysis continued to grow as we increased the embedding dimension for embedding dimensions up to 25. However, false nearest neighbour analysis (Kennel, Brown & Abarbenel 1992) indicates that the attractor should embed in eight dimensions.

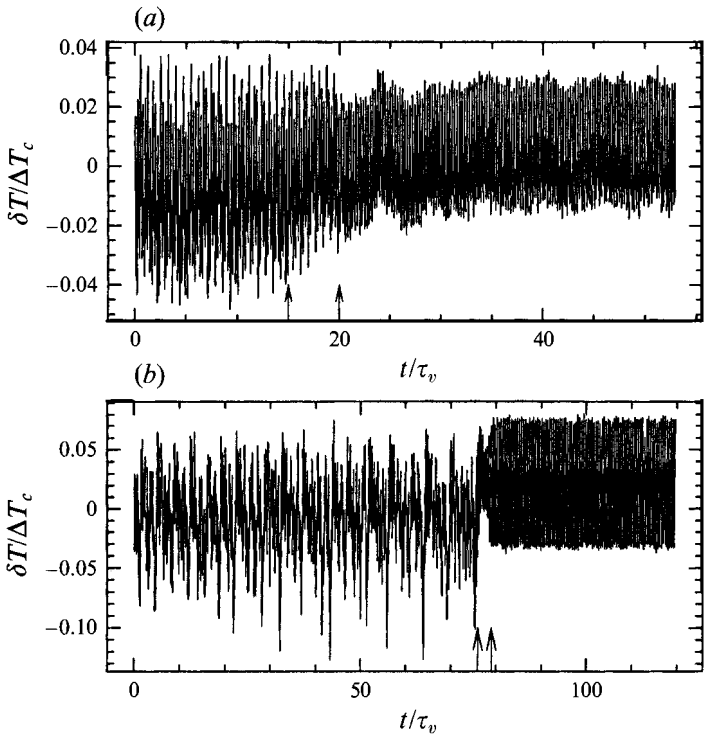

FIGURE 6. Spontaneous changes from chaotic to regular signals occur at fixed heat flux and demarcate at $r = 7.740$ (*a*) the transition QP→H and at $r = 9.379$ (*b*) the transition HQP→K. The heat flux was changed about $20\tau_v$ before the time origins in the figure. The arrows in each figure suggest how long it takes the pattern to change. The transitions occur about 1 and 3 horizontal diffusion times respectively after raising the heat flux.

2.1.2. *Destabilization*

We now turn to the experimental observations of bursting in superfluid mixture convection. After the sequence of transitions detailed above, figure 9(*a*) shows for $r = 15.85$ (with fixed heat flux) the time-dependence of ΔT after the onset of fully developed chaos. The instrumental noise is smaller by a factor of 10^3 than the amplitude of δT. Figures 9(*b*) and 9(*c*) show examples of the bursting that occurs as r is raised. The bursts are well-defined and occur more frequently for higher r. Bursts always increase ΔT and consequently decrease N.

For a given r, we take time series at a 2.5 Hz data acquisition rate for about 2 days and then count the number n and length b of each burst, as well as the length l of the time interval between bursts. Since the start and finish of any given burst is sharp and well-defined, the count is easily done by hand. Examples of a typical burst and a typical burst-free interval are marked in figure 9(*b*). The value of n ranges from 1 to 60 for $15.85 \leqslant r \leqslant 26.35$; n is sensitive to external noise and can be raised substantially at a given r by increasing the thermal fluctuations due to temperature regulation at the bottom plate thermal reservoir of the cell. Increasing the thermal fluctuations at the bottom plate tenfold increases the fraction of time spent bursting by about 30%.

In figure 10 we plot on log–log scales the average duration of a burst-free interval $\langle l \rangle$ versus $r - r_b$, where r_b is the scaled Rayleigh number for the onset of bursting.

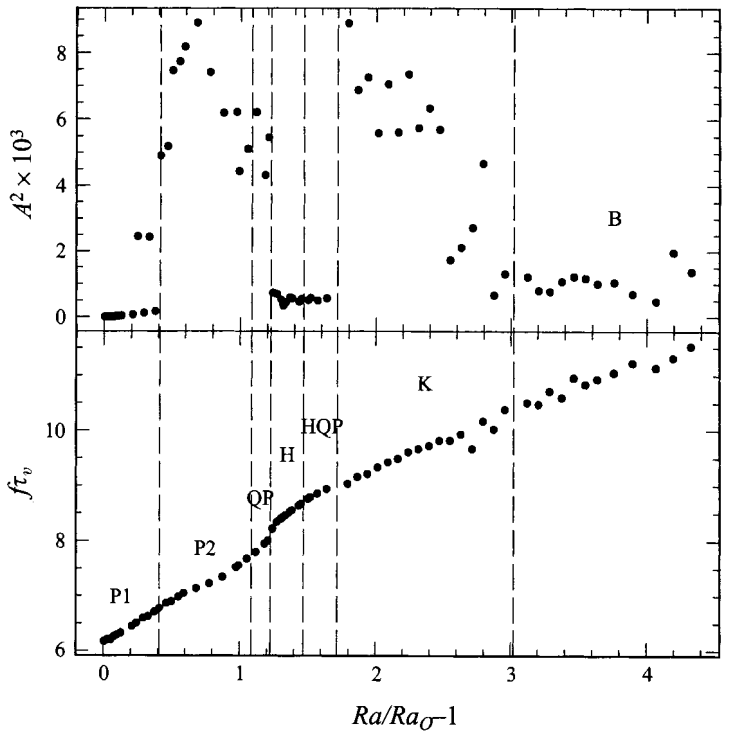

FIGURE 7. The amplitude and frequency of the Busse oscillation peak as a function of $Ra/Ra_O - 1$. The different regions are labelled as in figure 2.

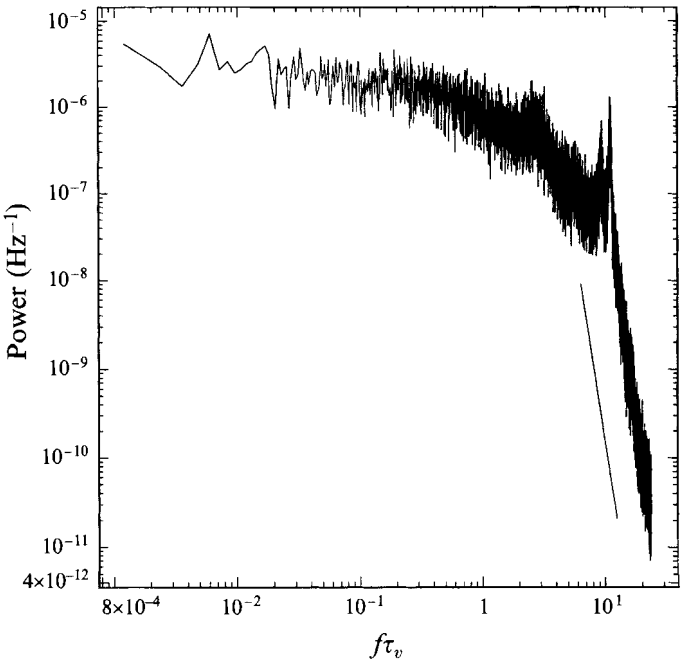

FIGURE 8. Power spectrum of the data in figure 9(*a*). The offset line has a slope of −8.8.

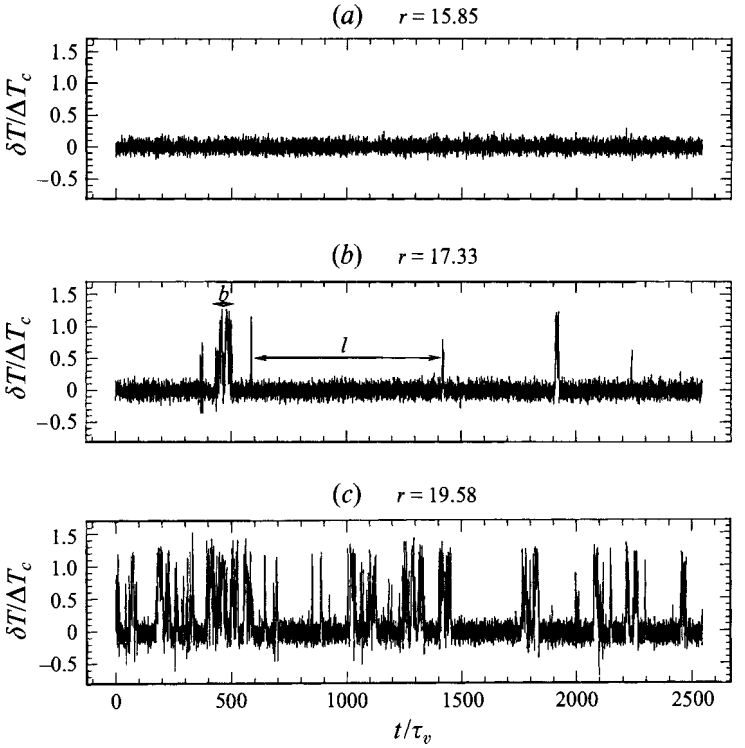

FIGURE 9. Time series illustrating bursting from a chaotic attractor. Each part shows every 20th point in a 20 hour data segment at the indicated value of r. In (*b*) b and l are typical examples of respectively a burst and an interval between bursts. The time axis origin is arbitrary. $\Delta T_c = 0.969$ mK and $\tau_v = 31.4$ s. Bursts always increase ΔT.

The error bars are $\pm\langle l\rangle/n^{1/2}$. The solid line is a fit of the data to a power law $\langle l\rangle = A_l(r-r_b)^{-\gamma}$. The fit is very good and gives an exponent $\gamma = 4.6 \pm 0.1$. Plotted in figure 10(*b*) are data for the average burst duration $\langle b\rangle$ versus $r - r_b$. It too follows a power low $\langle b\rangle = A_b(r-r_b)^{\delta}$. A fit gives $\delta = 2.2 \pm 0.1$. The two points at lowest r in the bottom of figure 10 are from runs that had only one burst in two days of data-taking. These two points were left out of the calculation of γ, as the time between bursts was not determined, but were included in that of δ.

The distributions of burst and interburst durations are shown in figure 11 for $r = 18.370$. This figure plots histograms of l and b from a run lasting 5 days and showing 210 events in each histogram. In §2.1.3 we discuss several models that reproduce aspects of these data, but the power-law behaviour of $\langle b\rangle$ and the distribution of bursting times is unpredicted from any model and raises the question of what kind of relation – if any – there should be between γ and δ, and what such a connection would imply about the structure of the changing attractor and the global phase-space.

2.1.3. *Possible models*

We are aware of two possible models for the bursting data. In the model of Grebogi, Ott, Yorke and coworkers an attractor grows with increasing r until it touches (at r_b) the stable manifold of a nearby unstable periodic orbit. This is termed a point of 'crisis' and leaves an unstable region through which orbits can leave the attractor. An

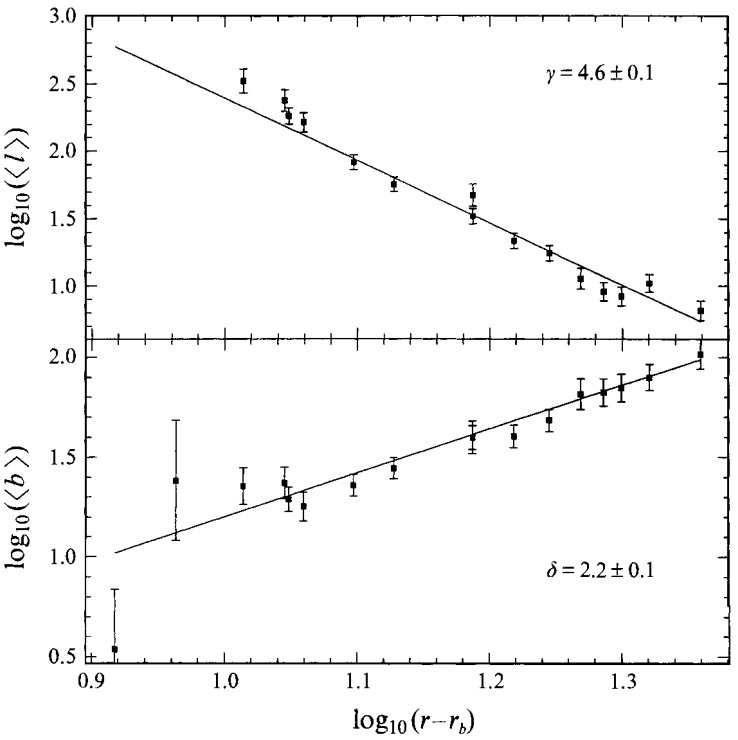

FIGURE 10. Log_{10} plots of the average duration of burst-free $\langle l \rangle$ and burst $\langle b \rangle$ intervals versus $\log_{10}(r - r_b)$. $\langle l \rangle$ and $\langle b \rangle$ are calculated from time series such as those of figure 9. Lines are least-squares fits of the data to power laws with the resulting exponents indicated. For $\langle l \rangle$ the amplitude of the power law fit $\log_{10} A_l = 7.0 \pm 0.1$; for $\langle b \rangle$ $\log_{10} A_b = -1.0 \pm 0.1$. From both fits $r_b = 13.9 \pm 0.4$ is obtained.

ejected orbit moves along the unstable manifold of the periodic orbit into the global phase-space and eventually returns to the chaotic attractor. The predicted behaviour just past a point of crisis is that, for the most part, the system will continue on the remnant of the strange attractor, as before, but will now make intermittent, often large, excursions into previously unused parts of phase-space with the average interval between excursions varying with $(r - r_b)$ as a power law (Grebogi *et al.* 1987; Grebogi, Ott & Yorke 1983). Since this crisis-induced intermittency is caused by interaction of the strange attractor with unstable manifolds, and since unstable periodic orbits (and their manifolds) are dense in any neighbourhood of a strange attractor, crisis-induced intermittency is a generic possibility for a chaotic attractor.

Another mechanism for producing intermittency in dynamical systems was originally developed for modelling turbulent wall layers (Aubry *et al.* 1988; Holmes 1990). The ideas rest upon the dynamical system obeying some symmetry. The symmetry in turn brings structural stability to heteroclinic cycles connecting limit sets, which can be chaotic sets. In the absence of perturbation, orbits are attracted onto one limit set or another. Stone & Holmes (1990) have shown for a model system of one homoclinic connection that almost any variety of random or deterministic perturbations will produce bursting, and they have calculated $\langle l \rangle$, which they call the mean passage time, as a function of the perturbation amplitude ϵ and the size of the largest unstable eigenvalue λ_u. The mean passage time in their model is $\langle l \rangle = K_0 + \lambda_u^{-1}(|\ln(\epsilon)| + K_1)$ where $\epsilon \ll 1$, and K_0 and K_1 are constants depending on the particulars of the model.

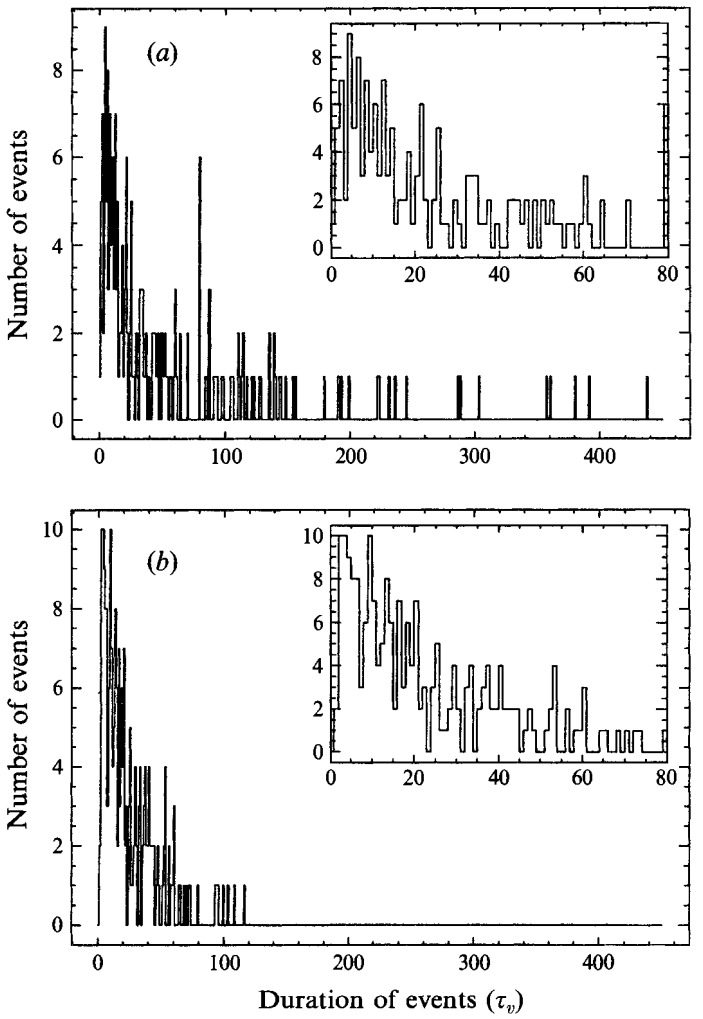

FIGURE 11. Histograms of (*a*) l and (*b*) b for $r = 18.370$ derived from a data run with 210 bursting events. Both distributions are peaked and (the l distribution particularly) skewed towards longer events. The insets are enlargements of the distributions nearer zero. The bin size for each histogram is $1\tau_v$.

Stone & Holmes also predict that the distribution of passage times should have an exponential tail. The present experimental histograms have an extended tail, but the number of events in a typical run, while sufficient to accurately calculate $\langle l \rangle$, are not numerous enough to confidently distinguish between distributions.

Both models qualitatively agree with aspects of the data, though neither model seems capable of addressing the data for the burst durations because both rely on linearizing about a point in phase-space. Modelling the bursts would seem to require a global analysis.

2.2. *Switching*

Our second example of chaotic attractor destabilization is a switching transition between two different chaotic attractors. For $\Gamma = 4.25$ and $Pr = 0.13$ ($T = 1.000$ K) steady convection loses stability to time-dependence at $r = 2.8$. Unlike the bursting,

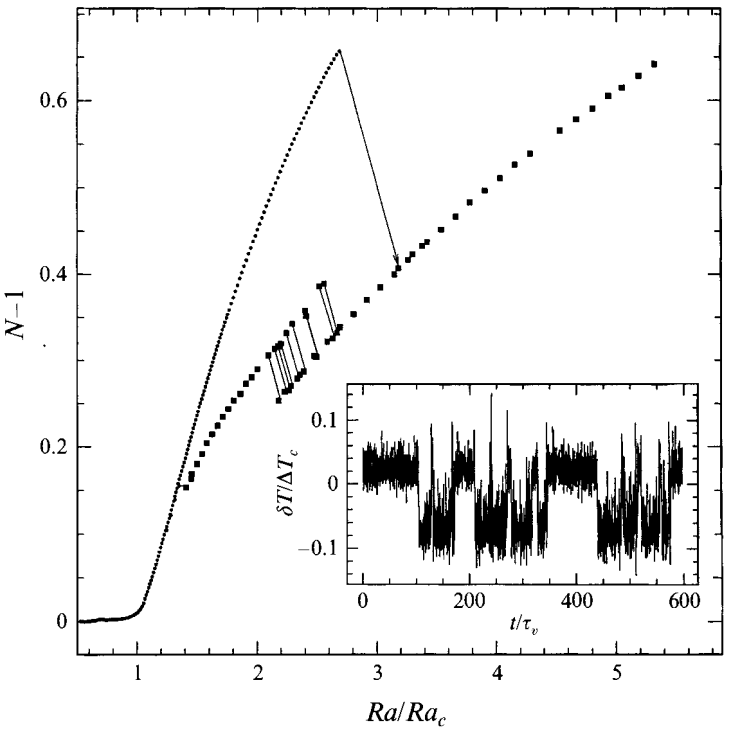

FIGURE 12. Nusselt curve for $Pr = 0.13$, $\Gamma = 4.25$, at which parameters switching occurs. The squares show time-dependent and the dots steady convection. Lines connecting squares indicate the state-to-state switching discussed in the text. The inset shows an example of switching between $(r, N-1) = (2.500, 0.2799)$ and $(2.399, 0.3345)$. $\Delta T_c = 8.654$ mK and $\tau_v = 7.05$ s.

where time-dependence begins as a periodic motion and with increasing r gradually becomes fully developed chaos, here the initial time-dependence is already chaotic. Figure 12 shows the Nusselt curve. The squares represent the branches of time-dependent convection; the dots are points of steady convection. The jump transition from steady to time-dependent convection occurs reproducibly at $r = 2.8$, as does the reverse jump transition from time-dependence to steady convection at $r = 1.45$.

On the time-dependent branches, as r is increased through the range $2.2 \lesssim r \lesssim 2.8$, the chaotic state with higher N loses stability to the one with lower N via switching between the states; the inset to figure 12 shows a sample time record. Positive δT corresponds to low N, and negative δT to high N. This time series is from the middle of the switching region. Spectra for the low- and high-N states are shown in figure 13. For $r < 2.2$ (and the system in the chaotic state) the fluid is always in the high-N state. As r is raised above 2.2, the system begins to switch back and forth between the high- and low-N states. As r is raised further, the system spends more and more time in the low-N state, until for $r > 2.8$ the transition is complete and the system remains in the low-N state. The solid lines in the figure connect paired high- and low-N states (and are not vertical because we use a constant heat flux). This transition is completely reversible: the Nusselt curve for the chaotic states is the same for increasing and decreasing r. We believe that this is the only experimental observation to date of switching of this type.

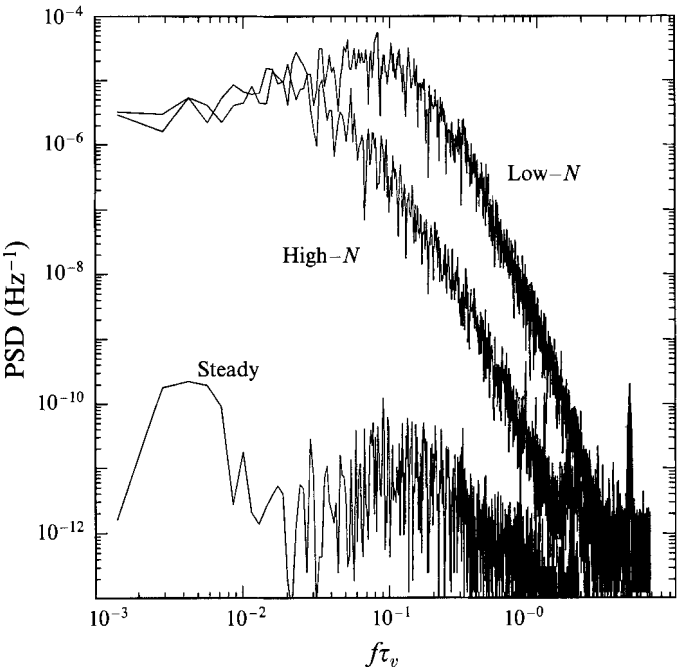

FIGURE 13. Typical spectra from the low- and high-N states, respectively at $r = 5.185$ and $r = 2.010$. Also shown for comparison is a spectrum from steady convection at $r = 1.316$. The acquisition rate for these data was 1.67 Hz. The feature at $f\tau_v = 4$ is an artifact of the temperature control.

A final experimental observation concerns the average frequency $\langle f \rangle$ or first moment of the power spectra for the switching states. Defined as

$$\langle f \rangle = \frac{\int f \mathrm{PSD}(f)\,\mathrm{d}f}{\int \mathrm{PSD}(f)\,\mathrm{d}f}, \tag{2.1}$$

where PSD(f) is the power spectral density at frequency f, $\langle f \rangle$ increases linearly with increasing r, as shown in figure 14. The squares are calculated from the spectra of the low-N state and the triangles are calculated from those of the high-N state. The line in figure 14 is a least-squares fit to the squares only and fits the data well. The $\langle f \rangle$ values calculated from the high-N state cluster around the line extended from the low-N state but do not follow it.

The analysis of Grebogi *et al.* (1987) and Grebogi, Ott & Yorke (1983) can also be adapted to the switching transition. The mechanism is for two attractors (only one of which is in use by the system) to grow as r is increased, until at the crisis the two attractors simultaneously touch at their mutual basin boundary. This leads to an overlap of the two attractors, which merge but remain *apparently* distinct for some range of r: the system will remain on one or the other of the previously distinct attractors for some, possibly long, period of time before switching suddenly to the remnant of the other attractor. The overlap becomes greater and greater as r increases, until the attractors are completely merged. Only in the presence of a global symmetry is it reasonable to expect the simultaneous touching of attractors, but more general (and complicated) scenarios can be devised by removing the symmetry requirement

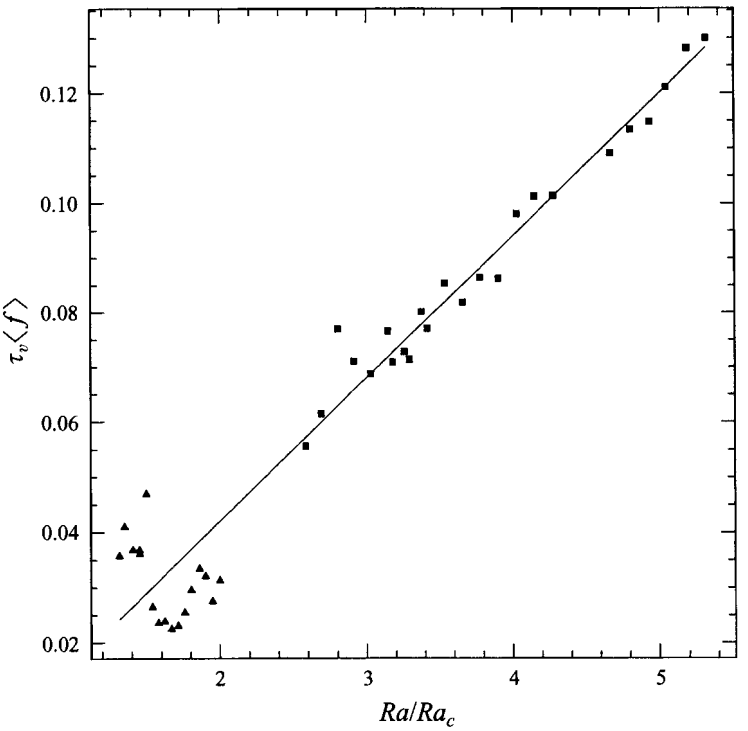

FIGURE 14. The scaled average frequency of the power spectrum versus r. The squares are for the low-N state and the triangles are for the high-N state. The least-squares fitted line shown is $\tau_v\langle f\rangle = 0.026r - 0.01$. The fit uses only the squares.

(Ott, private communication). In such a scenario, there are two chaotic sets: A_u associated with the upper Nusselt state, and A_l with the lower state. Below $r = 2.2$, A_u is an attractor, and A_l is a non-attracting chaotic set. At $r = 2.2$, A_u undergoes a crisis and destabilizes. Between $r = 2.2$ and $r = 2.8$, neither set is attracting by itself. Rather, both states are weakly unstable, so that the trajectory lingers near one or the other state for substantial times before moving to the the other set. At $r = 2.8$, A_l undergoes a stabilizing inverse crisis and becomes the attractor for the system.

3. Complexity near a codimension-2 point

The Prandtl number for superfluid mixtures can be set in the range $0.04 < Pr < 2$. In the upper part of this range, the first secondary instability encountered as Ra is raised well above Ra_c is the skewed-varicose instability. It is, at its onset, a stationary instability causing a periodic thickening and thinning of the convection rolls. The new roll shape, however, is accompanied by mean flows and is likely to initiate a pattern change by, for instance, nucleating a defect (Newell, Passot & Souli 1990). The end result of the skewed-varicose instability is that, starting from a parallel roll planform, one roll pair is 'consumed' and the system stabilizes at a smaller wavevector (Croquette 1989). At lower Pr the first secondary instability is the oscillatory instability (Clever & Busse 1974; Busse 1981). Ecke and coworkers (Mainieri, Sullivan & Ecke 1989; Deissler, Ecke & Haucke 1987) have used SMC to study the oscillatory instability in a cylindrical cell of unity aspect ratio but at smaller Pr than considered here. Others (Chiffaudel, Perrin & Fauve 19891; Libchaber, Fauve

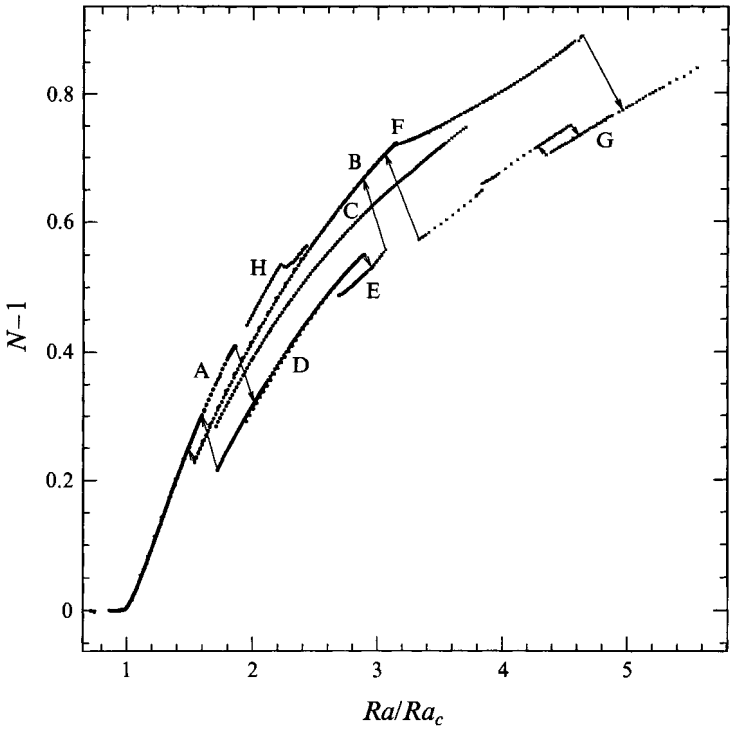

FIGURE 15. The Nusselt curve at $Pr = 0.23$ and $\Gamma = 8$ in the neighbourhood of the codimension-2 point, strongly showing the effects of competition between the skewed-varicose and oscillatory instabilities. Dots mark points of steady convection and crosses mark points of time-dependent convection. Branches A–D show only steady convection. Branch E is steady for $r < 2.85$, oscillatory otherwise. Branches F and G show only time-dependent convection. Arrows indicate the transitions made as the heat current is adiabatically changed.

& Laroche 1983) have used mercury ($Pr = 0.025$) to study oscillatory convection, but with the limitation to a single Prandtl number and a single aspect ratio (for a given experiment). In Part 1, finding the intersection of the skewed-varicose instability and the oscillatory instability at a Prandtl number close to that predicted was taken as additional evidence of the superfluid mixture convection–Rayleigh–Bénard convection correspondence. In this section we investigate the dynamical behaviour near the codimension-2 point (Guckenheimer & Holmes 1983), which has not previously been well characterized owing to the experimental difficulties of accessing such points (Brand, Hohenberg & Steinberg 1984; Rehberg & Ahlers 1985; Sullivan & Ahlers 1988).

3.1. *Complexity from competing instabilities*

The codimension-2 point of superfluid mixture convection, which lies near $Pr = 0.23$ ($T = 1.161$ K) for $\Gamma = 8.00$, shows a remarkably complex array of accessible states, as seen in the Nusselt data in figure 15. In what follows, the wavevector is kept close to critical by setting Γ to be an even integer. Wavevector changes (imposed through either two-fluid or mechanical means) presumably cause interesting modifications to the effects found below, but we leave those studies for the future.

At a given Ra, as many as four different states are reproducibly accessible, depending on the history of the system. The arrows in figure 15 show the path selected

Γ	d (cm)	τ_v (s)	f (Hz)	$f\tau_v$ (obs.)	$f\tau_v$ (pred.)
8 (branch E)	0.2849	6.2	0.03	0.2	10.2
8 (branch F)	0.2849	6.2	0.73	4.5	10.2
4	0.5747	25.1	0.14	3.5	10.2

TABLE 1. Frequencies of oscillatory states for $Pr = 0.23$. For comparison the predictions of Clever & Busse (1974), and Busse (1981) for q_c are also shown.

when the heat flux Q is adiabatically changed. At the first secondary instability the transition is from state A to state D. States B and C can be reliably found by applying heat pulses of specific duration (§3.3); branches A–D and H show only stationary convection. At higher Ra/Ra_c we still find multiple stable states: stationary and time-dependent states may be locally stable at the same Rayleigh number, the chosen state depending on the exact path taken. On branch E, for example, a forward Hopf bifurcation occurs at $Ra/Ra_c \approx 2.85$, but the transition from the stationary branch D is into the middle of the oscillatory region, and shortly after period-doubling branch E becomes unstable to branch B. Branch F begins similarly to the true oscillatory instability, and oscillatory branch F coexists with chaotic branch G. Branch G shows chaos at larger Ra/Ra_c, at lower Ra/Ra_c shows quasi-periodic transitions to chaos, and has other unusual features, such as a hysteresis loop. With decreasing Ra, branch G makes a transition onto steady branch B. Branch H was brought about by a sudden drop in ΔT which took the system from F to A (but still above the onset of convection). Subsequently when raising Ra to try to induce the transition terminating A, we found that A was stable until jumping onto B at $Ra/Ra_c = 2.42$.

This strikingly complex behaviour is presumably due to the competition between the skewed-varicose and oscillatory instabilities, and we emphasize that the Nusselt curve of figure 15 is *exactly* reproducible to experimental accuracy – and, in fact, most of the branches show overlaying data from several different runs.

Table 1 lists the frequencies of several simply periodic states along with oscillatory instability predictions for this Pr (Clever & Busse 1974). Figure 16 shows time series and power spectra illustrating the variety of time-dependence among the complex of states. As physical processes not accounted for in the calculations must become important near the codimension-2 point, it is not surprising that measured and predicted frequencies do not agree. None of the frequencies at $Pr = 0.23$ can be reasonably accounted for in the standard instability scheme.

3.2. *Complexity suppressed with decreasing* Γ

As Γ is lowered to 6 and then 4, while keeping the Prandtl number fixed at $Pr = 0.23$, regions of multi-stability still exist at and above the first secondary instability but their overall complexity lessens considerably as Γ decreases. At the first secondary instability for $\Gamma = 6$ (figure 17*a*) there are two states available from the initial steady branch A, both of which are time-dependent. The transition from the initial steady state was highly sensitive to the initial conditions; attempts to prepare identical steady states did not yield the same first secondary instability. The arrows in figure 17(*a*) locate the transitions for three different runs. The time-dependence of branches B and D and branch C of figure 17(*c*) are similar to the non-periodic 'noisy' states discussed in §4 although, in all other observed instances these states had the smallest Nusselt number of any accompanying states, time-dependent or steady (except of course the preconvective state). Here, branch B at $\Gamma = 6$ has higher N than oscillatory branch C.

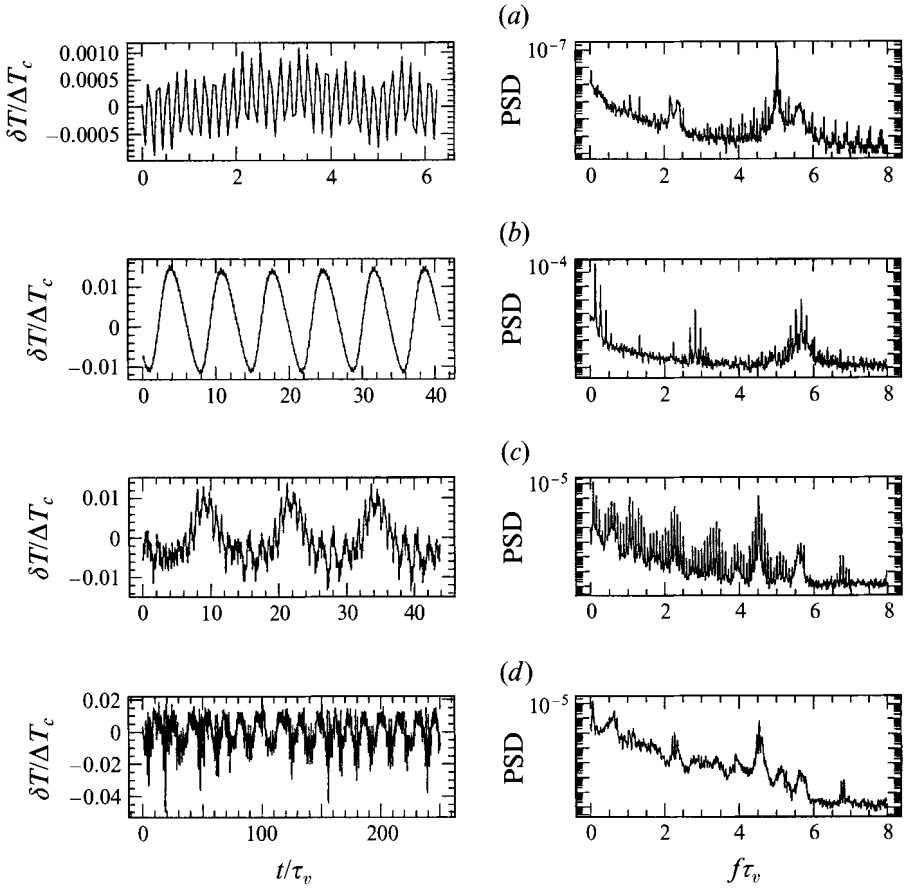

FIGURE 16. Examples of time-dependence near the codimension-2 point. The left-hand column shows time series taken at various points of figure 15; the right-hand column shows the corresponding power spectrum (PSD in units of Hz^{-1}) on log–linear scales. (*a*) Branch F: $r = 3.50$, $N - 1 = 0.746$; (*b*) branch F: 4.58, 0.882; (*c*) branch G: 4.51, 0.720; (*d*) branch G: 4.56, 0.726.

As the arrow indicates, branches B and D are connected by a jump transition which bypasses the periodic behaviour of branch C. State C is periodic with a forward Hopf bifurcation at $r = 3.1$. From there it undergoes a period-doubling-like sequence up to period-4. However, the sequence is interrupted before achieving period-8 and the component of the spectrum at $f/4$ becomes unexpectedly large.

At $\Gamma = 4$ (figure 17*b*) jump transitions at the first secondary instability go away altogether. Instead there is the 'fork' at $r \approx 8.5$ from which both the steady branch A and the periodic branch B can grow. If the point of instability is crossed by taking small (about 1%) steps in heat flux Q, then one stays on steady branch A, but if the instability point is crossed with larger (about 5%) steps in Q, then one crosses onto oscillatory branch B. By decreasing Q in small steps while on B one finds that B is a forward Hopf bifurcation beginning at the 'fork' with a dimensionless frequency at onset of 3.5.

One should compare figures 15 and 17. While it is still true that multiple stable states coexist at and above the first secondary instability for the three aspect ratios studied, the degree of complexity is severely depressed at lower Γ and is but a remnant of that evident in figure 15 for $\Gamma = 8$.

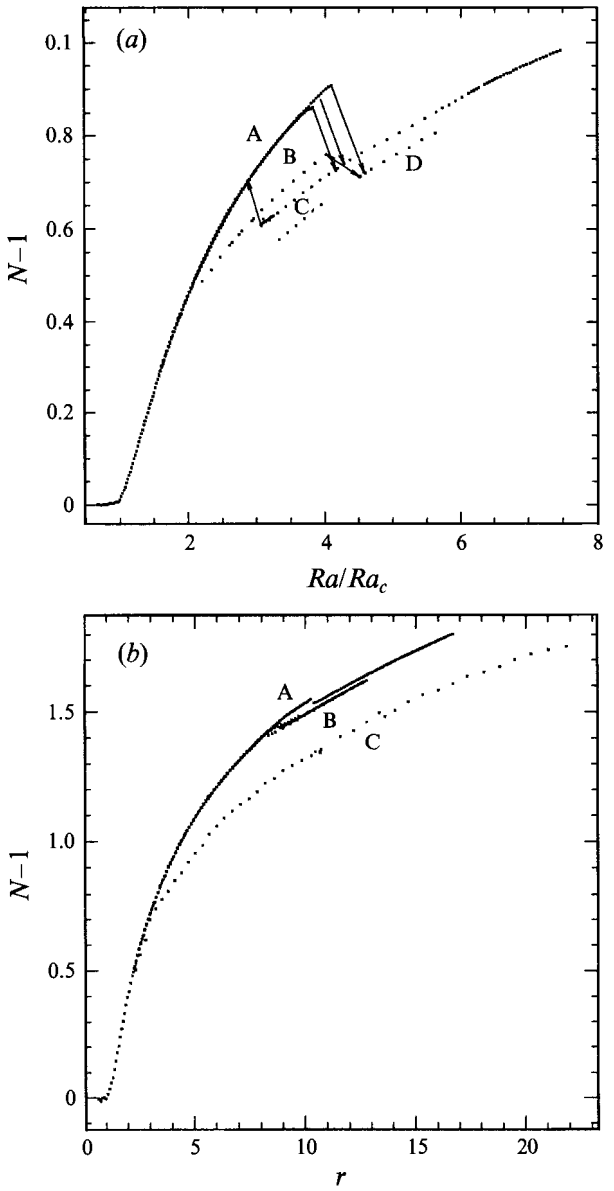

FIGURE 17. Nusselt curve near the codimension-2 point at $\Gamma = 6$ (*a*) and $\Gamma = 4$ (*b*). The effects of competition between the two instabilities still exist but the number and complexity of states are suppressed as Γ decreases. The different convective behaviours on the labelled branches are discussed in the text.

3.3. *Thermal pulses to initiate transitions*

For $Pr = 0.23$ and $\Gamma = 8$ there are three stable states accessible to the system from the end of branch A. If the Rayleigh number is raised adiabatically across the end of branch A, the system goes to branch D. By adiabatic, we mean a small step change in Q followed by sufficient time for the system to relax. On the other hand, if we change the heat step to a heat pulse (defined below), short pulses leave the system on A; longer pulses produce the same effect as a heat step. The transition finds branch B or C for narrow, non-overlapping windows of pulse length. Figure 18 shows the data.

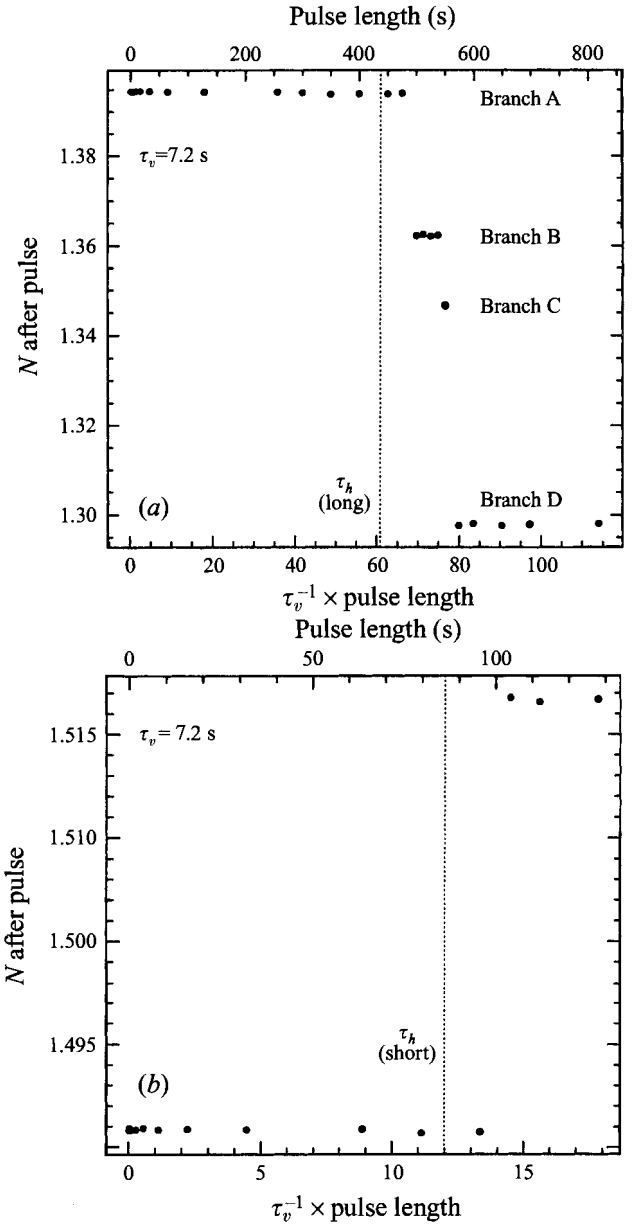

FIGURE 18. Thermal-pulse-induced transitions at $\Gamma = 8.0$, $Pr = 0.23$. Plotted here is the resulting Nusselt number after the pulse *vs.* the normalized pulse length. (*a*) Three steady states (B, C, D) are accessible from state A of figure 15. The length of a heat-current pulse determines which state is chosen by the fluid. The amplitude of the pulse is such that leaving it on causes A→D. The horizontal thermal diffusion time as reckoned from the long horizontal dimension is marked with a vertical dotted line. (*b*) A negative heat-current pulse applied to the lower end of Branch E causes E→D. The horizontal thermal diffusion time here is reckoned using the short side of the cell.

In figure 18(*a*) we plot the Nusselt number obtained after applying a heat pulse versus the pulse length normalized by τ_v. The unnormalized pulse length labels the top axis of the figure. Before application of each pulse, we arrange the system to be on branch A at $r = 1.809$, which is just below the termination point of branch A. The amplitude of the pulse is such that if we leave it on, we always obtain the transition A→D.

Upon application of a heat pulse, ΔT immediately increases (decreasing N), as if a transition were taking place. If the pulse is shorter than $65\tau_v$, then ΔT will decrease again after the pulse ends and return N to its original value. Pulses longer than $80\tau_v$ are equivalent to heat steps and branch D always results. In between 65 and 80 there are two non-overlapping windows within which pulses reproducibly cause transitions to branches B or C. The vertical dotted line in figure 18(*a*) marks the horizontal thermal diffusion time calculated with respect to the long side of the cell.

Figure 18(*b*) shows a plot similar to that of 18(*a*) but for the transition E→D. Here the dotted line marks the horizontal thermal diffusion time calculated using the *short* side of the cell for the characteristic length. The difference in pulse lengths between figures 18(*a*) to 18(*b*) needed to cause transitions may indicate that the latter case requires some propagation *along* roll axes while the former requires propagation *across* rolls.

In this section we have seen how the bifurcations near the anticipated codimension-2 point unfold with surprising richness. This rich behaviour vanishes away from the codimension-2 point (see Part 1) and diminishes with aspect ratio. Evidently, the coupling between various modes either stabilizes states which ordinarily are not stable, or makes accessible a variety of states which ordinarily are not accessible. Having three experimental parameters (Γ, Pr, Ra) also opens the possibility that this system may be able to experimentally access phenomena of codimension higher than 2. We leave this issue to future work.

4. Noisy state at small Γ and Pr: superfluid turbulence?

In investigating secondary instabilities, such as the oscillatory or skew-varicose, we encountered noisy states which are not simply related to either of these instabilities. These include at $Pr = 0.23$ branches B and D for $\Gamma = 6.00$ and branch C for $\Gamma = 4.00$. We consider one more example in figures 19 and 20. Figure 19 shows Nusselt data for $Pr = 0.14$ and $\Gamma = 4$, illustrating this unusual instability not predicted from linear stability calculations. The higher-N state is steady convection until the oscillatory instability, which begins at the cusp at $r = 4.814$. The noisy state is the time-dependent branch at lower N for $r > 1.5$. The chief characteristics of the new state are that it may be spontaneously excited from nearly anywhere along the initial branch of steady convection, and that time-dependence is large amplitude and irregular. This suggests that the state is not related to any of the linear instabilities of straight convection rolls. Figure 20 shows a typical 'noisy' time series with a time series from steady convection for comparison.

These unusual states have large-amplitude fluctuations of N with a broad characteristic peak and a f^{-4} fall-off of the power spectrum. The fall-off is similar to those states previously reported by Wheatley, Ecke and coworkers (Haucke *et al.* 1980; Ecke, Haucke & Wheatley 1987) at lower Pr and Γ in superfluid mixtures and by Ahlers & Behringer (1978) in pure ^{4}He at $Pr = 0.78$ and aspect ratios of $\Gamma = 4.7$, 5.3 and 57. It is interesting to note that even with the strenuous set of perturbations applied to the system in producing figure 15, these large-amplitude fluctuations were

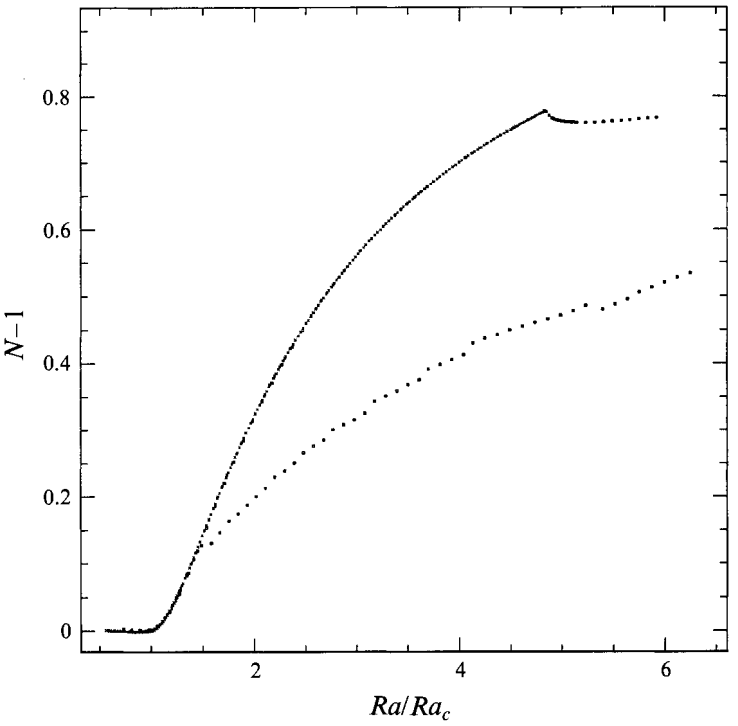

FIGURE 19. Nusselt curve for $Pr = 0.14$ and $\Gamma = 4.0$. The crosses (upper data) show steady convection, the squares time-dependent convection. The oscillatory instability occurs at $r = 4.814$. The low-N branch shows large-amplitude irregular fluctuations.

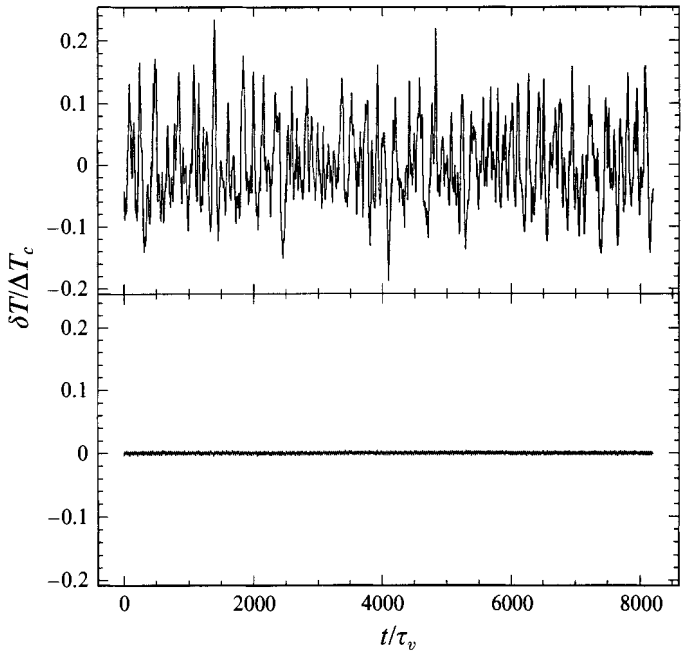

FIGURE 20. Time series (top) typical of the noisy state ($r = 5.230$), with a typical time series (bottom) from the steady branch ($r = 1.278$) for comparison. $\tau_v = 8.04$ s; $\Delta T_c = 6.849$ mK.

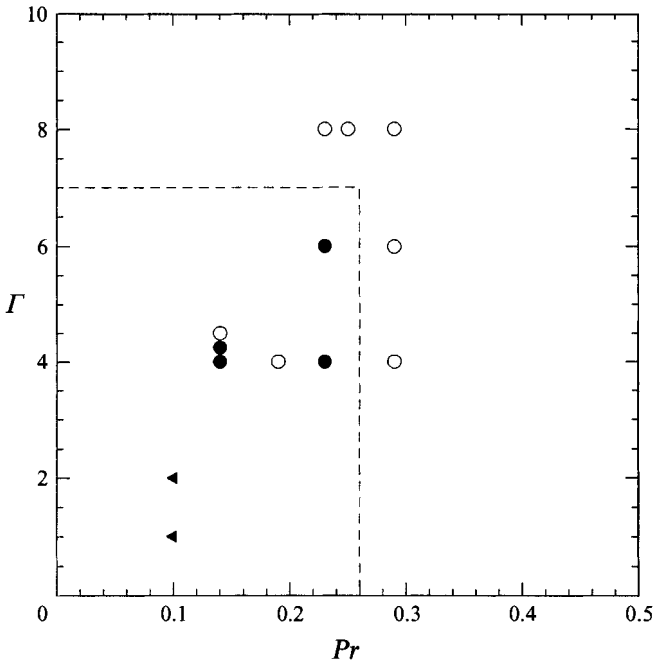

FIGURE 21. Occurrences of the noisy state in the Pr–Γ plane. The filled symbols indicate that the noisy state was excited; the open symbols that the noisy state was not excited. There is no differentiation between spontaneous and induced transitions to the noisy state. Triangles represent data for cylindrical and rectangular cells of $\Gamma = 1$, 2 and $Pr < 0.1$ (Haucke *et al.* 1981; Ecke *et al.* 1987). Not shown are the data of §6 for $Pr = 1.3$ and $\Gamma > 40$ for which the noisy state was never seen, or data for which Ra/Ra_c was not raised above 1.5 (e.g. the data of Part 1). The noisy state has never been observed outside the dashed box.

never once excited at $\Gamma = 8$. Yet for most Pr investigated by us at $\Gamma \leqslant 6$ this transition to the noisy state has always been observed after raising Ra not too much above Ra_c.

The noisy state has several properties in all the above examples: (i) it almost always has lower N for a given Ra than any other convective state (see however, branch B for $\Gamma = 6.00$, $Pr = 0.23$); (ii) it can be excited from another state but the reverse does not happen; (iii) the probability of exciting the noisy state increases if relatively large steps in Q are taken; (iv) the amplitude of the noise is relatively large, $\sim 0.1\Delta T_c$; (v) the noisy state always terminates well above the onset of convection and does so by a jump transition back to a steady convection branch; (vi) the spectra are broadband with power-law fall-offs; (vii) the noisy states occur only for low Pr and low Γ. This final point is made in figure 21 which shows where we observed the noisy state in a parameter space of Pr and Γ. Our data are given by circles, with closed circles indicating a point where the noisy state was seen and open circles a point where it was not seen. Notably, the noisy state was not seen for $\Gamma = 8$, nor was it seen for aspect ratios above 40 (and $Pr \approx 1$). The triangles in the figure are representative of results from Haucke *et al.* (1980) and Ecke *et al.* (1987). These authors, who used smaller Γ and Pr than here, reported noisy states close to the onset of convection. They found that their ability to excite the noisy state was a function of the history of their experiment. By cycling the mean temperature across the superfluid transition, they made the occurrence of the noisy state less probable. They interpreted these

observations to mean that the noisy state was driven by the presence of quantum vortices.

We suggest that the noisy states we observe may be related to another effect, however, such as a finite-amplitude instability which occurs for small Γ and Pr. In support of this hypothesis, we note that it is surprising that the noisy states do not occur at larger Γ in these experiments. Larger Γ implies larger counterflow velocity, and therefore an increased probability of nucleating superfluid vortices. Specifically, vortex generation is a function of the counterflow velocity $|\boldsymbol{v}_n - \boldsymbol{v}_s|$ which in turn consists of a non-convective part proportional to $\Delta T/d$ and a convective part. The counterflow velocity grows with increasing Ra and with increasing d^{-1}. Since $\Delta T_c \propto d^{-3}$, the non-convective counterflow velocity grows as d^{-4}. The convective counterflow presumably grows inversely as the height of the layer. In either case, we might expect the effect to be *more* likely to occur with increasing aspect ratio (since this implies decreasing d), which is the reverse of our observations. We note that Chiffaudel, Fauve & Perrin (1987), using mercury in a rectangular container with horizontal dimensions 6.25×4.25 (in units of d), did not report any such noisy state. However, this aspect ratio sits near the proposed noisy state boundary of figure 21. Clearly the existing data do not allow definitive conclusions on this state, and flow visualization would be very valuable.

5. Secondary bifurcation changes with aspect ratio detuning

It is also interesting to ask what would happen to the secondary instabilities if the aspect ratio were detuned from an even integer. A complete study of aspect ratio detuning is beyond the scope of the present work. However, we present some initial results which suggest the presence of interesting dynamical behaviour. This is also a case where changing Γ completely changes the secondary instability.

We show in figure 22 Nusselt data for $\Gamma = 7.8$ and $Pr = 0.19$. For the critical wavevector $q_{c\infty}$ obtained for an even integer Γ, rolls become unstable to the oscillatory instability upon increasing Ra (Part 1). Here, the non-integer aspect ratio detunes the critical wavevector by 2.5%, causing the initial steady convective state to become unstable to a finite-amplitude periodic state at $r = 1.756$. Typical time series for this state are given in figure 23, along with the oscillation period $\tau(r)$. The data for τ follow a power law $\tau = A_s(r - r_s)^{-\beta}$. Notably, a fit to the data gives $\beta = 0.75 \pm 0.02$. If Ra is increased past $r = 1.84$, a new stable state is reached.

A finite-amplitude periodic state of diverging period τ can occur after a saddle-node bifurcation, provided there is a mechanism to return the system trajectory to the neighbourhood of the former fixed point. A saddle-node bifurcation is a likely occurrence for a codimension-1 bifurcation. However, in that case, if the bifurcation parameter is $\mu \equiv r - r_s$, then τ is determined chiefly by the time to negotiate the region near the former fixed point, and $\tau \sim \mu^{-1/2}$, whereas our data show a 3/4 exponent. We can suggest two possible reasons for the larger exponent. First, the 1/2 exponent may pertain only asymptotically close to the bifurcation point: the present experiments may not have sampled the asymptotic regime. Or, second, this may be a different kind of saddle-node bifurcation.

The normal form for a standard saddle-node connection is

$$\mathrm{d}x/\mathrm{d}t = \mu + x^2. \tag{5.1}$$

For $\mu < 0$, this has a stable fixed point at $-(-\mu)^{1/2}$ and an unstable fixed point at $+(-\mu)^{1/2}$; for $\mu > 0$ it has no (real) fixed points. In this model, the relevant time scale

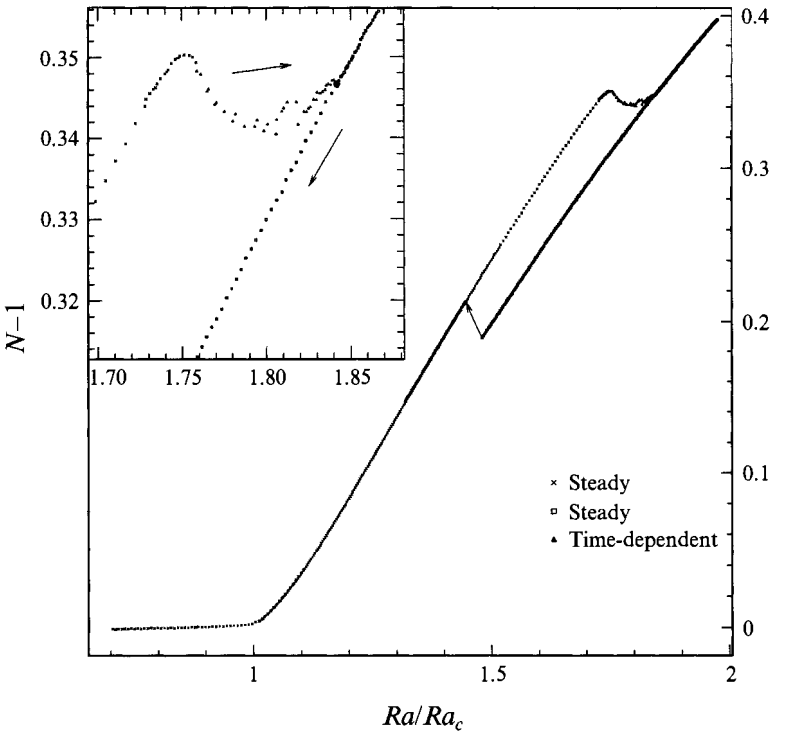

FIGURE 22. Nusselt curve showing a saddle-node connection beginning at $r = 1.756$ for $\Gamma = 7.8$, $Pr = 0.19$. The inset shows the bifurcation region on expanded scale. The time-dependent saddle branch connects two steady convection branches.

is proportional to $|\mu|^{-1/2}$. However, the data more closely resemble the model

$$dx/dt = \mu + x^4. \tag{5.2}$$

This has fixed points for $\pm(-\mu)^{1/4}$ for negative μ and no (real) fixed zeros for positive μ. For this form, the time scale goes as $|\mu|^{-3/4}$ in accord with the present experiments. However, there would have to be special circumstances, such as special symmetry, for such an unusual bifurcation to occur. This will be a topic for future study.

6. The transition to large aspect ratio convection

What happens at the onset of convection as the aspect ratio is made larger and larger? One effect has been recognized for some time: for smaller Γ, the sidewall drag substantially elevates the critical Rayleigh number above the value predicted for a horizontally infinite-layer. As Γ increases above about 8, the effect of the sidewalls lessens, and Ra_c approaches its infinite layer limit (Behringer 1985; Charlson & Sani 1975). This has been followed with investigations of the ordering effects of sidewalls. Meyer, Ahlers & Cannell (1987) used a low-Γ cell that reduced sidewall forcing and found at onset spatially disordered but still time-independent roll patterns. Other experiments visualizing up to 36 rolls (Croquette 1989) show that the onset of convection consists of ordered, stationary rolls.

The effect of primary interest in these experiments is the time-dependence arising *at the onset of convection* in very large-Γ experiments. Time-dependence at onset is specifically excluded by infinite-Γ calculations (Chandrasekhar 1961), but it is

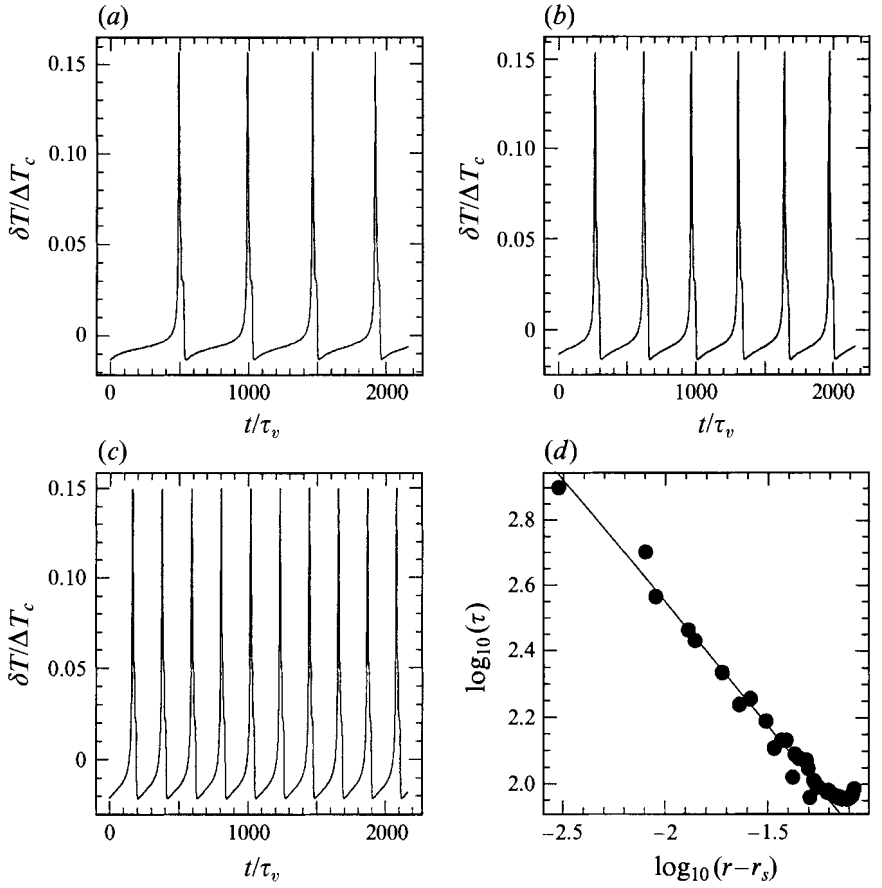

FIGURE 23. Saddle-node oscillations from figure 22. (*a*) $r = 1.761$; (*b*) $r = 1.766$; (*c*) $r = 1.775$. (*d*) Oscillation period τ versus $r-r_s$ on log–log scale, where r_s is the saddle bifurcation point. The solid line is $\tau = A_s(r-r_s)^{\beta}$ with $\log_{10} A_s = 1.05 \pm 0.02$, $r_s = 1.76 \pm 0.01$ and $\beta = -0.75 \pm 0.02$. Note that τ begins to increase just before jumping onto the lower steady branch of figure 22.

observed in experiments. For a $\Gamma = 57$ cylindrical cell, Ahlers & Behringer (1978) found non-stationary convection close to the onset of convection. Recent experiments with pressurized CO_2 gas in $\Gamma = 78$ and $\Gamma = 86$ cylinders report spiral chaos for $r \geqslant 1.4$ and large rotating spirals when the fluid is non-Boussinesq (Bodenschatz *et al.* 1991; Morris *et al.* 1993). At issue are the characteristics of this time-dependence and how it arises with systematic increase in Γ. In this section, we use the height changing capability of our experiment to investigate the changeover from order to disorder at the onset of convection as a function of increasing aspect ratio for $44 \leqslant \Gamma \leqslant 90$.

The Prandtl number for these experiments is held constant at $Pr = 1.30$ ($T = 2.086$ K), and the cell heights used in this section range from 1/4 to 1/2 mm. The length and width of the rectangular cell are respectively 2.284 and 1.013 cm (see Part 1), so that the horizontal thermal diffusion times are $\tau_{hl} = 686$ minutes and $\tau_{hs} = 138$ minutes across respectively the long and short sides of the cell.

One point concerning the number of rolls in the cell must be kept in mind. For classical fluids, the aspect ratio indicates the number of rolls in the cell. However, for the data in this section the cell height d is comparable to the superfluid dissipation length λ_o, so that superfluid effects do reduce the critical wavevector. For a fixed

Γ	d (mm)	λ_o/d	τ_v (s)	q_c	n
44	0.519	0.22	21.2	2.57	36
60	0.380	0.30	11.3	2.34	45
67	0.339	0.33	9.03	2.26	48
70	0.326	0.34	8.35	2.24	50
73	0.311	0.36	7.60	2.19	51
76	0.301	0.37	7.12	2.17	52
78	0.293	0.38	6.74	2.15	53
80	0.286	0.39	6.43	2.13	54
83	0.276	0.41	5.98	2.09	55
85	0.269	0.42	5.68	2.07	56
90	0.255	0.44	5.11	2.03	58

TABLE 2. The wavevector and number of rolls at the onset of convection for very large aspect ratios. At $T = 2.087$ K, the superfluid dissipation length $\lambda_o = 0.11$ mm. q_c is the critical wavevector expected from the calculations of Part 1 and n is the number of rolls at this wavevector that would fit into the cell assuming the rolls are parallel and aligned along the short side of the cell. d is the cell height. Also tabulated is the vertical thermal diffusion time τ_v for a thermal diffusivity of 1.27×10^{-4} cm^2 s^{-1}.

cell length, rolls with longer wavelengths mean fewer rolls. Table 2 lists the expected number of rolls n and their wavevector at onset q_c. Without superfluid effects $n \approx \Gamma$ and $q_c \approx 3.12$. In the table $n = \pi^{-1}\Gamma q_c$, rounded to the nearest integer. For $\Gamma > 60$, the wavevector reduction can be 25–35%. We have characterized in detail superfluid effects through the calculations and experiments in Part 1, and we emphasize that a reduction in q_c and an elevation of Ra_c are the only superfluid effects near the onset of convection.

The wavevector reduction may also be of some advantage in these experiments. At this Pr, the infinite-Γ calculations have the skew-varicose as the relevant instability. For $q_c = 3.12$ the instability occurs at $r = Ra/Ra_c \approx 1.4$, while for $q_c = 2.2$ the boundary is pushed up to $r \approx 4$ (although superfluid effects may shift the stability boundaries). Until encountering a secondary instability, we expect ordered, stationary convection, and the wavevector reduction should allow a larger Rayleigh number range, without interference from secondary instabilities, in which to look for deviations from stationary convection.

Our probe for disorder consists of examining time records of ΔT. All time series are digitized at a 2.5 Hz acquisition rate and Fourier transformed to obtain a power spectrum. In considering these time series, we use 'fluctuations' to characterize broadband temporal variations of the temperature difference, and 'oscillations' to characterize slow periodic variations of the temperature difference relative to the mean ΔT. The difference is illustrated in figure 24, where the data are scaled by the temperature difference at the onset of convection, ΔT_c. Fluctuations are changes δT in time about a constant mean ΔT. Oscillations, on the other hand, are coherent time-dependence of ΔT itself. Making this distinction, we find three regimes at the onset of convection as Γ increases.

(*a*) At smaller Γ, the fluctuation amplitude remains constant below and above onset, i.e. fluctuations show the instrumental noise level of the experiment. There are no oscillations (figure 24*a*).

(*b*) At moderate Γ, the fluctuation amplitude is constant or increases slightly as

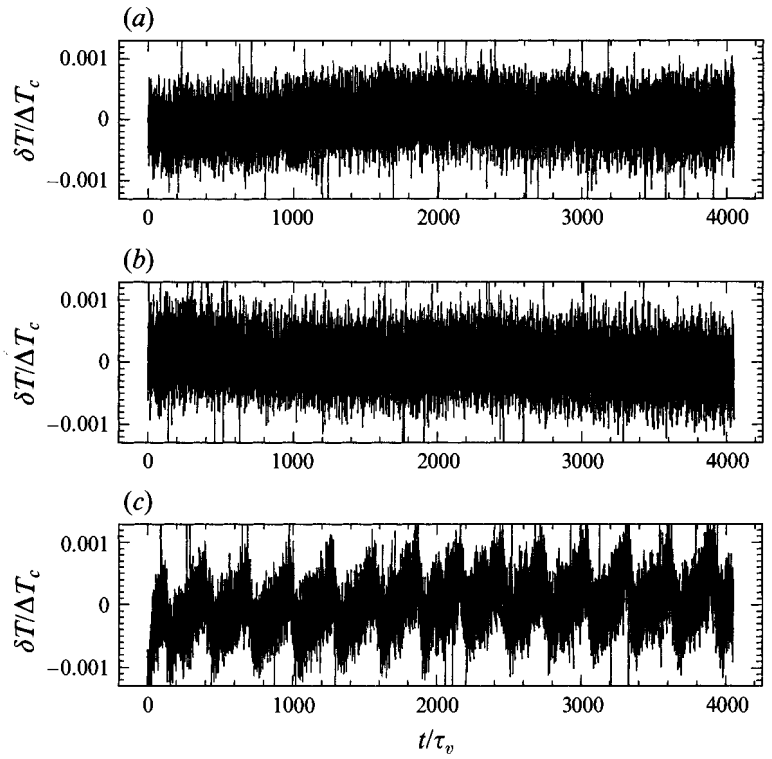

FIGURE 24. Example time records for $\Gamma = 70$. There are 50 rolls. (*a*) Below onset at $r = 0.949$. (*b*) fluctuations at $r = 1.308$. The signal amplitude in (*b*) is larger than in (*a*). (*c*) Oscillations at $r = 1.365$. At this aspect ratio and temperature, $\Delta T_c = 7.152$ mK and $\tau_v = 8.35$ s. The drifts in (*a*) and (*b*) occur because these experiments are near the limits of their temperature accuracy.

r increases above onset. The chief feature is a hysteretic transition to coherent oscillations at $r = 1.3$–1.6, the exact point depending on Γ (figure 24*c*).

(*c*) At larger Γ, the fluctuation amplitude increases continuously with r above onset and is correlated with the Nusselt number. There are again no oscillations (figure 24*b*).

Item (*a*) is not surprising: it affirms that at onset convection is steady and a large number of rolls form. Item (*c*) is similar to the data of Ahlers & Behringer (1978) who measured the r.m.s. deviation of temperature fluctuations in a $\Gamma = 57$ cylinder: at large enough aspect ratio the fluid is non-stationary whenever it is convecting. Item (*b*) is a new result of these experiments. There is a regime for aspect ratios between 60 and 85 where coherent oscillations in the fluid occur near the onset of convection. There is a crossover between ordered, stationary behaviour at onset for low Γ and temporal disorder for Rayleigh numbers arbitrarily close to (but above) the onset of convection for large Γ.

To quantify the growth of the average fluctuation amplitude about ΔT, we have chosen, from several possibilities, to calculate the integral of the power spectrum or the total power defined as

$$P = \int_{f_c}^{f_{Ny}} \mathrm{PSD}\, \mathrm{d}f, \tag{6.1}$$

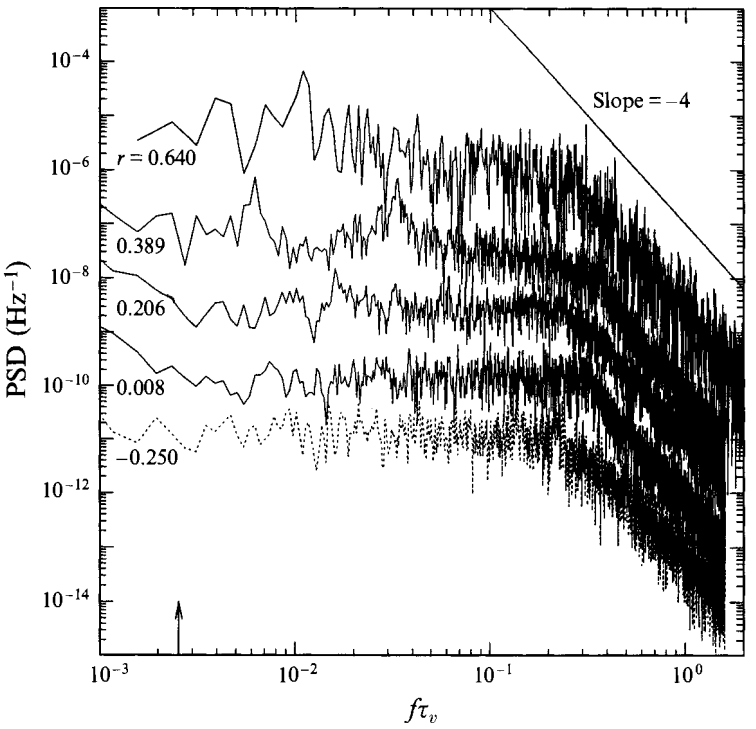

FIGURE 25. Spectra at $\Gamma = 90$ for increasing $r = Ra/Ra_c - 1$. For clarity each spectrum is offset 1 decade from the spectrum preceding it in r, except for the preconvective spectrum shown with a dotted line. The numbers to the left give r for each spectrum. As r increases, the total power in the spectrum increases, but the spectral shape stays constant. The arrow indicates the low-frequency cut-off f_c used in calculating P.

where PSD is the power spectral density, f_{Ny} is the Nyquist frequency, and f_c is a low-frequency cut-off. Spectra illustrating the increase of fluctuations and the oscillations are shown respectively in figures 25 and 26. The cut-off is needed because of small drifts in the time series, which can have an effect near zero frequency. The cut-off eliminates spurious drift effects from P. The cut-off frequency is the same for all data in this section and is marked with an arrow in figure 25. The use of a fixed cut-off may in some cases underestimate P at larger r.

Without oscillations the spectra from which P is calculated all have the same shape. Figure 25 shows examples from $\Gamma = 90$ over the entire accessible range of r. The spectral shape is flat for several decades with a 'knee' frequency near one third of the vertical diffusion time. Above the knee, the spectrum falls off as f^{-4}. Similar fall-offs are seen at smaller Γ in figure 26. Note that the knee frequency decreases with increasing Γ, even though the fluid characteristic frequency τ_v^{-1} increases with decreasing d. The lock-in amplifier output contains a low-pass filter with an f^{-4} (12 dB/octave) roll-off and a 3 s time constant. In the most extreme case, $\Gamma = 90$, the knee occurs at $f\tau_v \approx 0.3$, or $f \approx 0.06$ Hz. Conversely, the instrumental cut-off of 0.3 Hz corresponds, for $\Gamma = 90$, to $f\tau_v = 1.7$. Referring to figure 25, the instrumental low-pass cut-off is nearly 6 times the observed knee frequency, so we conclude that the attenuation and roll-off above the observed knee frequencies is not due to the lock-in.

Figure 27(*a–c*) shows plots of N and P as functions of r. P is normalized by its average value below onset, P_b. In these plots the crosses denote N and are labelled on

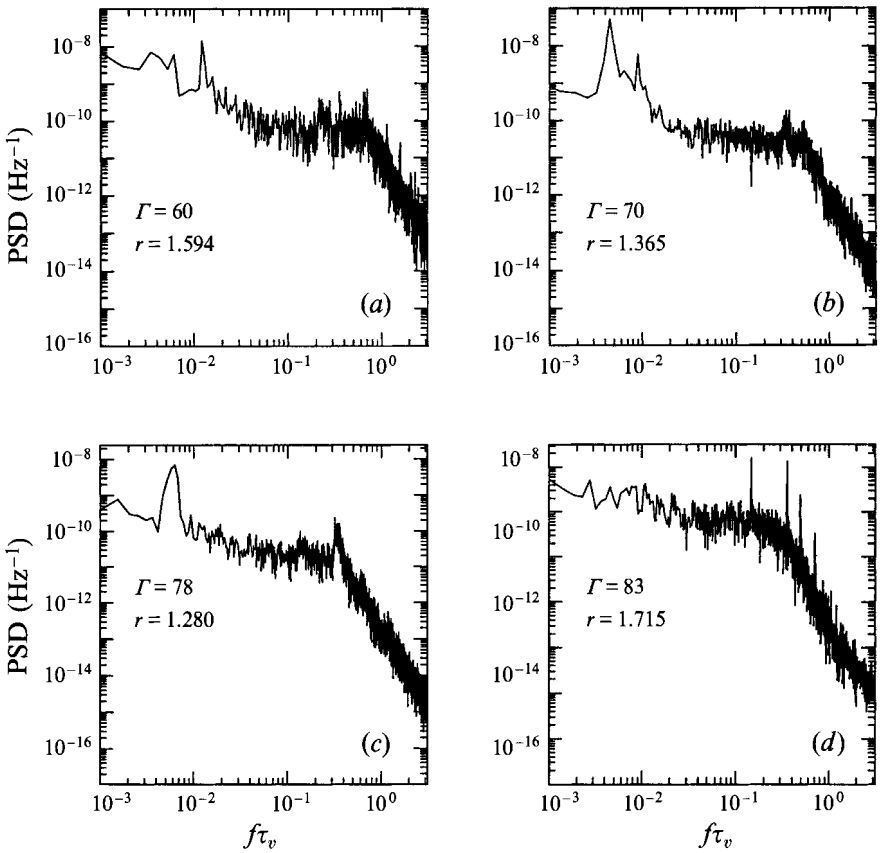

FIGURE 26. Spectra at several large aspect ratios showing oscillations near the onset of convection. See table 2 for τ_v at each Γ. In (*a*) there are spectral peak(s) at dimensionless frequencies of 0.012; in (*b*) at 0.0044 with a harmonic at 0.0089; in (*c*) at 0.006; and in (*d*) at 0.147, 0.355 and above. There is also always some spectral 'activity' at the knee frequency. This is a common feature in our data but does not have a clear explanation. The knee frequency also decreases with increasing Γ.

the left-hand axis, and the squares denote P/P_b and are labelled on the right-hand axis. Filled squares show points with only fluctuations, and open squares show points with oscillations. It is not hard to distinguish whether oscillations exist for a given run. Beyond visual inspection, a more sensitive criterion for deciding on the existence at a given r of oscillations is to check the spectrum for peaks (figure 26).

At $\Gamma = 44$, which corresponds to 36 rolls (table 2), figure 27(*a*) shows that we have the behaviour expected from steady convection. The Nusselt number is 1 in the absence of convective motion and rises sharply above 1 when convection begins. Thermal fluctuations are the same size above and below the onset of convection and are due to instrumental noise. There is steady convection at least up to $r = 2$. At $r = 2$, the signal goes through a long chaotic transient, at the end of which it is again steady but at a reduced Nusselt number. This is characteristic of the skew-varicose instability (Motsay, Anderson & Behringer 1988). We conclude that at $\Gamma = 44$ we see the same behaviour near and above onset as is seen for lower Γ: a stationary set of rolls, most likely approximately parallel to each other and aligned along the short side of the cell.

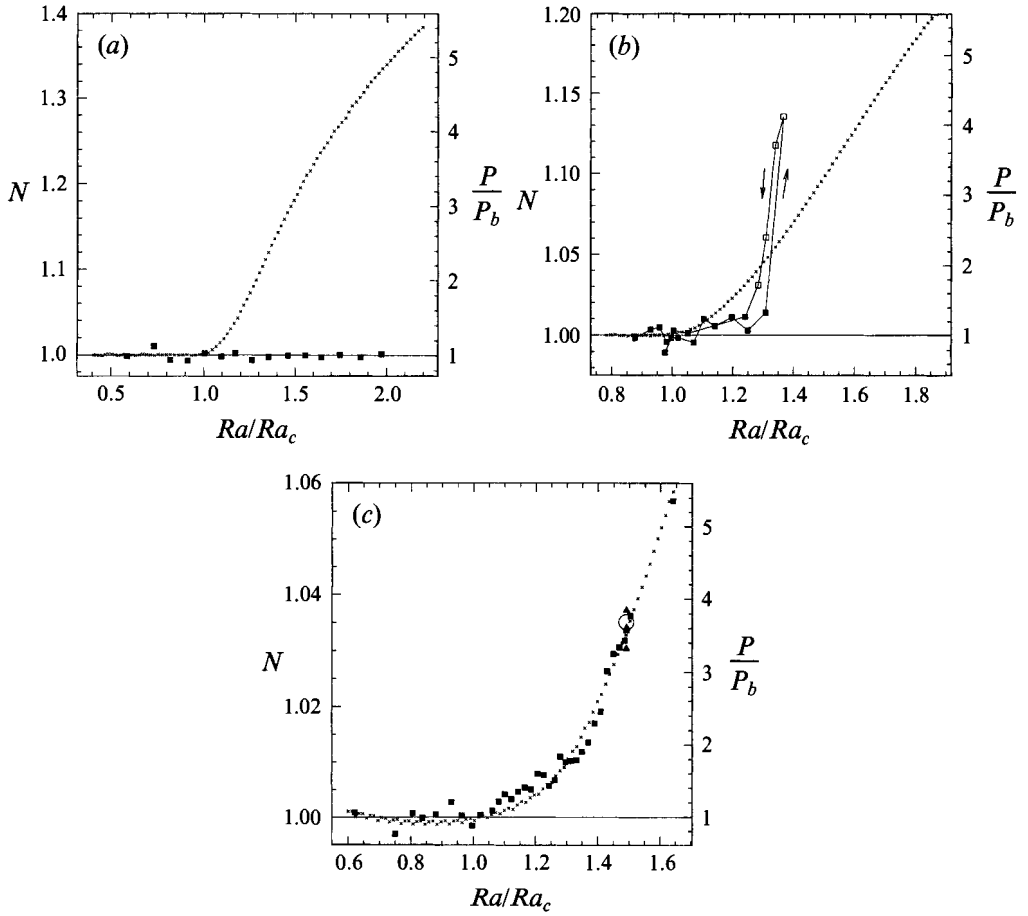

FIGURE 27. Nusselt number and noise power as a function of r for (*a*) $\Gamma = 44$, (*b*) $\Gamma = 70$, (*c*) $\Gamma = 90$. The crosses are Nusselt data and go with the scale on the left. The solid squares are the integral of the power spectrum normalized by its average value below the onset of convection and go with the scale on the right. In (*b*) open squares denote the presence of a sharp spectral feature. Arrows indicate data taken when raising or lowering r and the presence of hysteresis. In (*c*) the five triangles are the power calculated from consecutive 1 τ_{hl} segments of a run unperturbed for 5 τ_{hl}. The large open circle is the power calculated from the entire unperturbed run.

Unexpected behaviour begins as Γ increases to 60 and the number of rolls increases to 45. A hysteretic transition to oscillations occurs at $r \approx 1.7$. The fluctuation power, though, does not appear to increase above its background level. Similarly, for 50 rolls ($\Gamma = 70$), this transition occurs near $r = 1.35$ and involves larger-amplitude oscillations than at $\Gamma = 60$. The fluctuation amplitude increases slightly above its background value.

With the addition of five more rolls ($\Gamma = 90$), the correlation of power with Nusselt number becomes apparent. For $n = 58$ rolls, the power increases directly in proportion to the Nusselt number. Figure 28 shows this point explicitly by plotting P/P_b versus N. The data fit a straight line well. Noteworthy also at $\Gamma = 90$ is that there are no oscillations, as there were at every other aspect ratio investigated above 44.

A final point concerns the question of relevant time scales. The oscillation periods vary somewhat with Γ but are always on the order of $1000\tau_v \approx 20\tau_{hs} \approx 5\tau_{hl}$. Clearly,

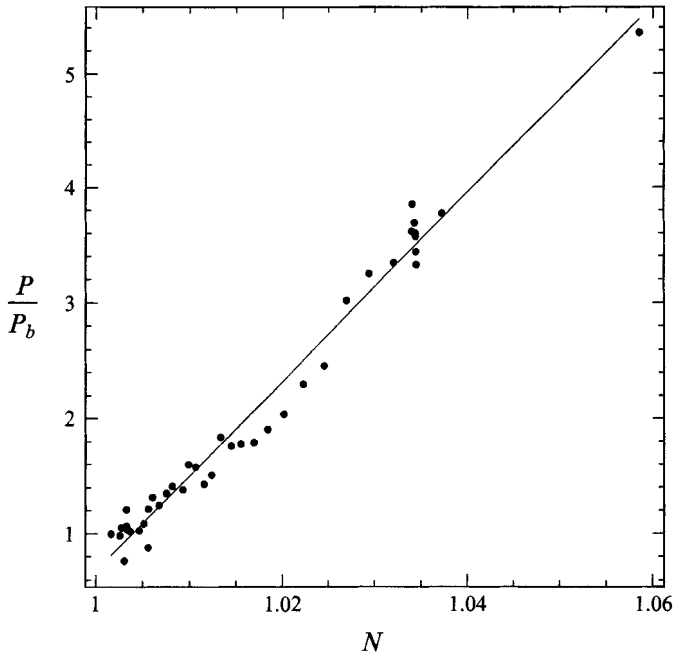

FIGURE 28. At $\Gamma = 90$ the Nusselt number and integrated spectral power are correlated. The line is a least-squares fit to the data for $P/P_b > 1$.

the horizontal diffusion time is the important time scale here. However, each square point in figure 27 represents a time series approximately 1 τ_{hl} long. This is not long enough to unequivocally guarantee that measurements made after raising the heat current are made on a fully relaxed system. Unfortunately, the transfer of liquid helium into the dewar every 2 days produces more of a perturbation than changing the heat current: we cannot let the experiment sit undisturbed indefinitely. To partially address this problem, and to spot any trends in the power as a function of time, we have taken data undisturbed for the full 2 days between transfers, then calculated P from consecutive $1\tau_{hl}$ segments of the data. The five triangles in figure 27(*c*) are the integrated power from such segments out of a time series of total length 5 τ_{hl}. The large open circle is P calculated from the entire run. Segments 1, 3 and 4 fall nearly on top of each other; segment 2 is slightly above and segment 5 slightly below the average. It is also relevant that we observe oscillations for weeks at a time ($15\tau_{hl}$–$30\tau_{hl}$): after a transfer perturbation, the system will relax back into the same oscillatory state with same mean Nusselt number. This evidence is consistent with the system being fully relaxed while we take data.

To conclude this section, we note the following points. As the number of rolls at the onset of convection is increased from 36 to 58, there is a changeover from ordered, stationary convection to disordered, time-dependent convection. Between the fully ordered and fully disordered states there is a crossover region that takes the addition of about 20 rolls to cross. At the beginning of the crossover region there are hysteretic transitions to coherent oscillations near the onset of convection. The Rayleigh number at which oscillations begin increases as Γ increases, while the fluctuation amplitude grows slowly or not at all. By the end of the crossover region the amplitude of disordered thermal fluctuations grows proportionally to the Nusselt number, while the onset of oscillations is pushed out to larger r and is no longer

hysteretic. For a large enough number of rolls, the noise power is amplified as soon as a convective velocity field exists, and the fluctuation amplitude is directly proportional to the convective amplitude. At $\Gamma = 60$, no fluctuations are discernible, whereas they are clearly present for $\Gamma = 70$. About 50 rolls seems to set the length scale at which the interior of the fluid can no longer feel the ordering effects of the sidewalls. We are left with the question of what sets this number?

7. Summary, conclusions, and future directions

This survey has focused on regions of low to moderate Pr and Γ and on the high-Γ region with $Pr \approx 1$. The regimes studied were chosen to address the dynamics of rolls near the codimension-2 point, the effects of aspect ratio on the oscillatory and skewed varicose instabilities, and the transition to near-onset chaotic flow. Conclusions on the individual topics are detailed throughout the paper. The survey has highlighted the richness and variety of the convective instabilities at low to moderate Pr. The survey is necessarily incomplete: large regions of Pr–Γ space remained unexplored (cf. figure 1). Even so, two themes seem to appear repeatedly: bifurcations with symmetry (attractor destabilization, saddle node), and the dramatic changes caused by increasing the number of degrees of freedom (codimension-2, large Γ).

Much exploration and characterization remains. In some cases, such as the effect of Γ on secondary instabilities, we uncovered intriguing dynamics, which we have not yet fully explored. On the theoretical side, we have shown that superfluid effects are small at onset when $\lambda_\circ/d$ is small. It is reasonable to expect that the secondary instabilities are also little changed from the standard RBC instabilities in that case. However, as $\lambda_\circ/d$ grows, the instability boundaries are likely to shift and unanticipated effects may emerge. Finally, the present experiments have not yielded the convection patterns; information in this regard would be extremely valuable.

This work has been supported by the NSF under grants DMR-9017236 DMR–9321791.

REFERENCES

AHLERS, G. & BEHRINGER, R. P. 1978 The Rayleigh-Bénard instability and the evolution of turbulence. *Supp. Prog. Theor. Phys.* **64**, 186–201.

AUBRY, N., HOLMES, P., LUMLEY, J. L. & STONE, E. 1988 The dynamics of coherent structures in the wall region of a turbulent boundary layer. *J. Fluid Mech.* **192**, 115–173.

BEHRINGER, R. P. 1985 Rayleigh-Bénard convection and turbulence in liquid helium. *Rev. Mod. Phys.* **57**, 657–687.

BERGÉ, P., DUBOIS, M., MANNEVILLE, P. & POMEAU, Y. 1980 Intermittency in Rayleigh–Bénard convection. *J. Phys. (Paris) Lett.* **41**, L341–345.

BODENSCHATZ, E., BRUYN, J. R. DE, AHLERS, G. & CANNELL, D. S. 1991 Transition between patterns in thermal convection. *Phys. Rev. Lett.* **67**, 3078–3081.

BRAND, H. R., HOHENBERG, P. C. & STEINBERG, V. 1984 Codimension-2 bifurcations for convection in binary fluid mixtures. *Phys. Rev.* A **30**, 2548–2561.

BUSSE, B. H. 1981 Transition to turbulence in Rayleigh-Bénard convection. In *Hydrodynamic Instabilities and the Transition to Turbulence* (ed. H. L. Swinney & J. P. Gollub), pp. 97–137. Springer.

CHANDRASEKHAR, S. 1961 *Hydrodynamic and Hydromagnetic Stability*. Dover.

CHARLSON, G. S. & SANI, R. L. 1975 Finite amplitude axisymmetric thermoconvective flows in a bounded cylindrical layer of fluid. *J. Fluid Mech.* **71**, 209–229.

CHIFFAUDEL, A., FAUVE, S. & PERRIN, B. 1987 Viscous and inertial convection at low Prandtl number; Experimental study. *Europhys. Lett.* **4**, 555–560.

CHIFFAUDEL, A., PERRIN, B. & FAUVE, S. 1989 Spatiotemporal dynamics of oscillatory convection at low Prandtl number: Waves and defects. *Phys. Rev.* A **39**, 2761–2764.

CLEVER, R. M. & BUSSE, F. H. 1974 Transition to time-dependent convection. *J. Fluid Mech.* **65**, 625–645.

CROQUETTE, V. 1989 Convective pattern dynamics at low Prandtl number: Part I. *Contem. Phys.* **30**, 113–133.

DEISSLER, R. J., ECKE, R. E. & HAUCKE, H. 1987 Universal scaling and transient behaviour of temporal modes near a Hopf bifurcation. *Phys. Rev.* A **36**, 4390–4401.

DUBOIS, M., RUBIO, M. A. & BERGÉ, P. 1983 Experimental evidence of intermittencies associated with a subharmonic bifurcation. *Phys. Rev. Lett.* **51**, 1446–1449.

ECKE, R. E., HAUCKE, H. & WHEATLEY, J. C. 1987 Convectively driven superfluid turbulence in dilute solutions of ^{3}He-superfluid-^{4}He. *Can. J. Phys.* **65**, 1322–1327.

GOLLUB, J. P. & BENSON, S. V. 1980 Many routes to turbulent convection. *J. Fluid Mech.* **100**, 449–470.

GREBOGI, C., OTT, E. & YORKE, J. A. 1983 Crises, sudden changes in chaotic attractors and transient chaos. *Physica* **D7**, 181–200.

GREBOGI, C., OTT, E. ROMEIRAS, F. & YORKE, J. A. 1987 Critical exponents for crisis-induced intermittency. *Phys. Rev.* A **36**, 5365–5380.

GUCKENHEIMER, J. & HOLMES, P. 1983 *Nonlinear Oscillations, Dynamical Systems, and Bifurcations of Vector Fields.* Springer.

HAUCKE, H., ECKE, R. E., MAENO, Y. & WHEATLEY, J. C. 1984 Noise-induced intermittency in a convecting dilute solution of ^{3}He in superfluid ^{4}He. *Phy. Rev. Lett.* **53**, 2090–2093.

HAUCKE, H., MAENO, Y., WARKENTIN, P. & WHEATLEY, J. 1980 Time-dependent thermal convection in dilute solutions of ^{3}He in superfluid ^{4}He. *J. Low Temp. Phys.* **44**, 505–533.

HOLMES, P. 1990 Can dynamical systems approach turbulence? In *Whither Turbulence? Turbulence at the Crossroads* (ed. J. L. Lumley). Springer.

KENNEL, M. B., BROWN, R. & ABARBENEL, H. D. I. 1992 Determining embedding dimension for phase-space reconstruction using a geometrical construction. *Phys. Rev.* A **45**, 3403–3411.

LIBCHABER, A., FAUVE, S. & LAROCHE, C. 1983 Two-parameter study of the routes to chaos. *Physica* **7D**, 73–84.

MAINIERI, R., SULLIVAN, T. S. & ECKE, R. E. 1989 Two-parameter study of the quasiperiodic route to chaos in convecting ^{3}He-superfluid-^{4}He mixtures. *Phys. Rev. Lett.* **63**, 2357–2360.

MANNEVILLE, P. 1990 *Dissipative Structures and Weak Turbulence.* Academic Press.

METCALFE, G. 1991 Using superfluid mixtures to probe convective instabilities. PhD thesis, Duke University.

METCALFE, G. & BEHRINGER, R. P. 1996 Convection in ^{3}He–superfluid-^{4}He mixtures. Part 1. A Boussinesq analogue. *J. Fluid Mech.* **307**, 269–296.

MEYER, C. W., AHLERS, G. & CANNELL, D. S. 1987 Initial stages of pattern formation in Rayleigh-Bénard convection. *Phys. Rev. Lett.* **59**, 1577–1580.

MORRIS, S. W., BODENSCHATZ, E., CANNELL, D. S. & AHLERS, G. 1993 Spiral defect chaos in large aspect ratio Rayleigh–Bénard convection. *Phys. Rev. Lett.* **71**, 2026–2029.

MOTSAY, R. W., ANDERSON, K. E. & BEHRINGER, R. P. 1988 The onset of convection and turbulence in rectangular layers of normal liquid ^{4}He. *J. Fluid Mech.* **189**, 263–286.

NEWELL, A. C, PASSOT, T. & SOULI, M. 1990 The phase diffusion and mean drift equations for convection at finite Rayleigh numbers in large containers. *J. Fluid Mech.* **220**, 187–252.

POMEAU, Y. & MANNEVILLE, P. 1980 Intermittent transition to turbulence in dissipative dynamical systems. *Commun. Math. Phys.* **74**, 189–197.

REHBERG, I. & AHLERS, G. 1985 Experimental observation of a codimension-two bifurcation in a binary fluid mixture. *Phys. Rev. Lett.* **55**, 500–503.

STONE, E. & HOLMES, P. 1990 Random perturbations of heteroclinic attractors. *SIAM J. Appl. Maths* **50**, 726–743.

SULLIVAN, T. S. & AHLERS, G. 1988 Hopf bifurcation to convection near the codimension-two point in a ^{3}He-^{4}He mixture. *Phys. Rev. Lett.* **61**, 78–81.

THEILER, J. 1987 Efficient algorithm for estimating the correlation dimension from a set of discrete points. *Phys. Rev.* A **36**, 4456–4462.